PHYSICAL REVIEW D **92**, 123526 (2015)

New reaction rates for improved primordial D/H calculation and the cosmic evolution of deuterium

Alain Coc[*]

Centre de Sciences Nucléaires et de Sciences de la Matière (CSNSM), Univ. Paris-Sud, CNRS/IN2P3,
Université Paris–Saclay, Bâtiment 104, F-91405 Orsay Campus, France

Patrick Petitjean,[†] Jean-Philippe Uzan,[‡] and Elisabeth Vangioni[§]

Institut d'Astrophysique de Paris, UMR-7095 du CNRS, Université Pierre et Marie Curie,
98 bis bd Arago, 75014 Paris, France
and Sorbonne Universités, Institut Lagrange de Paris, 98 bis bd Arago, 75014 Paris, France

Pierre Descouvemont[∥]

Physique Nucléaire Théorique et Physique Mathématique, C.P. 229, Université Libre de Bruxelles (ULB),
B-1050 Brussels, Belgium

Christian Iliadis[¶]

University of North Carolina at Chapel Hill, Chapel Hill, North Carolina 27599-3255, USA
and Triangle Universities Nuclear Laboratory, Durham, North Carolina 27708-0308, USA

Richard Longland[**]

North Carolina State University, Raleigh, North Carolina 27695, USA
and Triangle Universities Nuclear Laboratory, Durham, North Carolina 27708-0308, USA

(Received 2 October 2015; published 22 December 2015)

Primordial or big bang nucleosynthesis (BBN) is one of the three historically strong evidences for the big bang model. Standard BBN is now a parameter-free theory, since the baryonic density of the Universe has been deduced with an unprecedented precision from observations of the anisotropies of the cosmic microwave background radiation. There is a good agreement between the primordial abundances of ^{4}He, D, ^{3}He, and ^{7}Li deduced from observations and from primordial nucleosynthesis calculations. However, the ^{7}Li calculated abundance is significantly higher than the one deduced from spectroscopic observations and remains an open problem. In addition, recent deuterium observations have drastically reduced the uncertainty on D/H, to reach a value of 1.6%. It needs to be matched by BBN predictions whose precision is now limited by thermonuclear reaction rate uncertainties. This is especially important as many attempts to reconcile Li observations with models lead to an increased D prediction. Here, we reevaluate the $d(p,\gamma)^3$He, $d(d,n)^3$He, and $d(d,p)^3$H reaction rates that govern deuterium destruction, incorporating new experimental data and carefully accounting for systematic uncertainties. Contrary to previous evaluations, we use theoretical *ab initio* models for the energy dependence of the S factors. As a result, these rates increase *at BBN temperatures*, leading to a reduced value of $\mathrm{D/H} = (2.45 \pm 0.10) \times 10^{-5}$ (2σ), in agreement with observations.

DOI: 10.1103/PhysRevD.92.123526 PACS numbers: 26.35.+c, 98.80.Ft

I. INTRODUCTION

The standard hot big-bang model is supported by three pieces of observational evidence: the cosmic expansion (the Hubble law), the cosmic microwave background (CMB) radiation, and primordial or big bang nucleosynthesis (BBN). There is a good agreement between primordial abundances of ^{4}He, D, ^{3}He, and ^{7}Li deduced from observations and from primordial nucleosynthesis calculations. It is worth remembering that BBN has been essential in the past, first to estimate the baryonic density of the Universe and give an upper limit on the number of neutrino families. The number of light neutrino families was later determined from the measurement of the Z^0 width by LEP experiments at CERN. The observations of the anisotropies of the cosmic microwave background by WMAP [1], and more recently the Planck [2,3] space missions, enabled the extraction of cosmological parameters and, in particular, the baryonic density of the Universe.

---

[*] coc@csnsm.in2p3.fr
[†] ppetitje@iap.fr
[‡] uzan@iap.fr
[§] vangioni@iap.fr
[∥] pdesc@ulb.ac.be
[¶] iliadis@unc.edu
[**] richard_longland@ncsu.edu

It was the last free parameter in BBN calculations, now measured with an uncertainty of less than 1%: $\omega_b = 0.02225 \pm 0.00016$[1] [3]. Higher precision standard BBN predictions are now needed for comparison with primordial abundances deduced from observations.

Calculations of the ^{4}He primordial abundance are in agreement with those deduced from observations in HII (ionized hydrogen) regions of compact blue galaxies [4]. Contrary to ^{4}He, ^{3}He is both produced and destroyed in stars, and thus its abundance evolution as a function of time is not well known and is difficult to compare with predictions. It is well known that BBN calculations of ^{7}Li [5–8] overpredict the observations by a factor of ≈ 3. This is the so-called "lithium problem," which has not found a satisfactory solution yet [9,10] (see also Ref. [11]). Promising ideas revolve around stellar physics or exotic physics, now that a nuclear physics solution is highly unlikely [12]. Deuterium's most primitive abundance is determined from the observation of very few cosmological clouds at high redshift, on the line of sight of distant quasars. Recent observations of damped Lyman-α (DLA) systems at high redshift show a very small dispersion of deuterium abundance values, leading to a 1.6% uncertainty on the mean value that is marginally compatible with BBN predictions.

Here, we will focus on the reevaluation of the most important BBN reaction rates for deuterium nucleosynthesis. Sensitivity studies (e.g., Refs. [7,13]) have shown that the $d(d,n)^3$He, $d(d,p)^3$H, and $d(p,\gamma)^3$He reactions are the most influential for the D/H predicted abundance: a 10% variation of their rates induces a relative variation of −5.5%, −4.6%, and −3.2%, respectively, of D/H. Concerning these reactions, since the most recent dedicated BBN evaluations of reaction rates [13–15], new experiments were performed [16,17]. On the contrary, no new experiment concerning the $d(p,\gamma)^3$He reaction has been performed, and its rate uncertainty (5%–8% [15,18]), according to Di Valentino *et al.* [19], now dominates the error budget of D/H predictions.

The recent NACRE-II[2] [21] evaluation provides new rates for these reactions. However, too few explanations are given regarding the data selection, fitting, and uncertainty estimation. Therefore, the published evaluated rates of these reactions are not suited to reach the precision required for BBN calculations. Here, we reevaluate the $d+d$ rates, to take advantage of the new precise measurement by Leonard *et al.* [16], together with the $d(p,\gamma)^3$He rate. We use these new rates to derive BBN abundances and associated uncertainties. We will then compare our new BBN predictions for deuterium with high-redshift observations in the framework of cosmic evolution models.

For our reevaluations, we chose a compromise between adopting the most recent, and more precise measurements only [i.e., LUNA [22] for $d(p,\gamma)^3$He and Leonard *et al.* [16] for $d+d$], on the one hand, and including all available experimental data in the fit, on the other hand. The main difficulty in this analysis is the treatment and extraction of systematic uncertainties. Another difficulty is the choice of the fitting functions: polynomials [13,20], splines [23], or R-matrix [15] have been used. For these three reactions we chose instead, as fitting functions, results from nuclear reaction models. It has the advantages of smoothing the accidental fluctuations in experimental data and providing a better interpolation of the data. In the case of a single data set, the fitting process is reduced to a normalization, but when several data sets have to be considered, a global normalization is required, which is discussed in the Appendixes. In addition, we found that, by using the theoretical ratio of $d(d,n)^3$He and $d(d,p)^3$H cross sections, it was possible to identify inconsistent data sets in an objective way.

This article is organized as follows. In Secs. II and III, we discuss the normalization of $d(p,\gamma)^3$He, $d(d,n)^3$He, and $d(d,p)^3$H theoretical S factors to experimental data. (The normalization method is presented in Appendix A, and the experimental data are discussed in Appendixes B and C.) In Sec. IV, we present the new reaction rates (tabulated in Appendix D) and the Monte Carlo method for nucleosynthesis calculations. BBN results are discussed in Sec. V, while the cosmic deuterium evolution is presented in Sec. VI. Finally, we show in Sec. VII that the new precise D/H observations put a strong constraint on the proposed solution to the lithium problem.

II. THE D(p,γ)^{3}He S FACTOR

The sensitivity of the D/H abundance ratio to $d(p,\gamma)^3$He rate variations is [7]

$$\frac{\Delta(\mathrm{D/H})}{\mathrm{D/H}} = -0.32\frac{\Delta\langle\sigma v\rangle_{d(p,\gamma)^3\mathrm{He}}}{\langle\sigma v\rangle_{d(p,\gamma)^3\mathrm{He}}}. \tag{2.1}$$

Therefore, a precision of $\lesssim 5\%$ is required for the rate, to match the 1.6% uncertainty in the observed value. In the Appendixes, we detail our choice of the data sets we included in our analysis. Data sets for which no systematic uncertainty was quoted (or when the quoted uncertainty was too large) were excluded from the fit. Nevertheless, they are reported in the figures and tables, where the scatter of values gives an idea of their systematic uncertainties.

NACRE [20] used data from Refs. [24–33], plus a few high energy experiments and a polynomial fit, while Descouvemont *et al.* [15] (DAACV hereafter) used a slightly different set of data from Refs. [22,24–26,32–36] and included the data from Ref. [22] (post-NACRE; from

---

[1] We note $\omega_b \equiv \Omega_b \cdot h^2$, with Ω_b the ratio of the baryonic to critical density and h the Hubble constant in 100 km s^{-1} Mpc^{-1} units.

[2] In the following, we use "NACRE" when referring to the Angulo *et al.* [20] original evaluation and "NACRE-II" when referring to the recent sequel by Xu *et al.* [21].

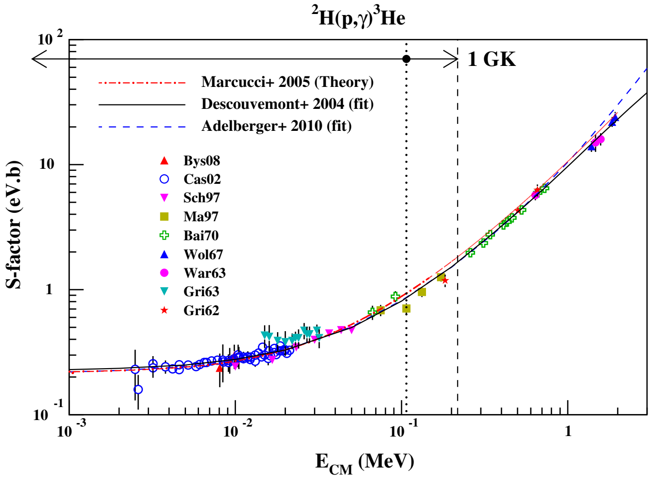

FIG. 1 (color online). S-factor data considered in our evaluation compared to previous fits [15,18] or theory [37]. (See references in Table I.) The arrows and dashed and dotted vertical lines correspond to the Gamow window at a temperature of 1 GK.

LUNA) with an R-matrix fit. Figure 1 summarizes all the experimental data that we collected (see Appendix B), together with the fitted curves from Refs. [15,18] and the theoretical S factor from Marcucci *et al.* [37]. This is the theoretical S factor that we renormalize to the data, as described in Appendix A: the renormalization factor (α) and the associated uncertainty ($\Delta\alpha$) are obtained by χ^2 minimization [see Eqs. (A2) and (A3)]. The results ($\alpha \pm \Delta\alpha$) of our analysis for the nine data sets [22,24–26,32–34,36,38] can be found in Table I, column 3. Column 5 of the same table lists the systematic uncertainties (ϵ), available for only the four most recent data sets, to which we restrict our subsequent analysis. The systematic uncertainties are quadratically added to the normalization factor uncertainties [Eq. (A8)] before calculating the recommended normalization factor.

Figure 2 displays the normalization factors α from Table I, with error bars that incorporate the systematic uncertainty [Eq. (A8)] when available. One observes that when the systematic uncertainties on normalization are included for the four selected data sets, the dispersion of values of normalization factors becomes compatible with the error bars. Hence, a simple weighted average [Eq. (A7)] and associated uncertainty [Eq. (A9)] seems to us sufficient, leading to $\alpha = 0.9900 \pm 0.0368$ (Fig. 2) with a reduced chi square of $\chi^2_\nu = 0.71$. We checked that the method used in some other evaluations (e.g., Ref. [14]), and discussed in Appendix A 2, gives a very close value, $\alpha = 0.9844 \pm 0.0366$ [from Eq. (A6) minimization].

The zero energy theoretical S factor is given by $S(0) = 0.21545$ eV b, which, after renormalization ($\alpha = 0.9900 \pm 0.0368$), leads to $S(0) = 0.213 \pm 0.008$ eV b, in excellent agreement with the value $S(0) = 0.214^{+0.017}_{-0.016}$ eV b determined by Adelberger *et al.* [18]. Hence, experimental data do not favor a *global* increase by a factor of ≈1.10 ± 0.07 as proposed by Di Valentino *et al.* [19] and the Planck Collaboration [3] to better reproduce the Cooke *et al.* [39] deuterium observations (see Sec. VI). Even when considering the experimental data that were not included in our fit (because their systematic uncertainties were not quantified; see Fig. 2), there is no evidence for such a global enhancement. Figure 3 displays the experimental S-factor data, divided by the corresponding theoretical values [37]. Except for Griffiths *et al.* [25], low energy data are in excellent agreement with our recommended average (horizontal solid lines). At higher energies, previous phenomenological fits [13,15,18] closely follow the experimental data points (Fig. 3). In particular, they are attracted by the Bailey *et al.* data [34] with very small error bars (Fig. 2) but unknown systematic uncertainty (see Appendix B). For this reason we do not use these data in our fit. As it is based on a theoretical model [37] that predicts the shape of the S factor, our fit is little influenced by the data of Ma *et al.* [33] with relatively large uncertainties (systematic uncertainties are not shown in Fig. 3 but displayed in Fig. 2). This explains that at BBN energies, the scarce data generally fall below our recommended average. Hence, while at low energy, our S factor is in excellent agreement

TABLE I. Results for the $d(p,\gamma)^3$He reaction[a].

		$d(p,\gamma)^3$He		
Reference	N	α	χ^2_ν	ϵ
Bys08 [38]	3	1.0365 ± 0.1457	0.1360	≤ 0.08
Cas02 [22]	51	1.0243 ± 0.0092	0.5792	≈0.045
Sch97 [36]	7	0.9657 ± 0.0062	11.1799	0.09
Ma 97 [33]	4	0.8469 ± 0.0381	1.1052	0.09
Bai70* [34]	11	0.9108 ± 0.0143	0.3874	n.a.
Wol67* [32]	3	0.9202 ± 0.0514	0.2967	n.a.
War63* [26]	3	0.8867 ± 0.0581	0.2994	n.a.
Gri63* [25]	12	1.1749 ± 0.0535	0.2322	n.a.
Gri62* [24]	3	0.9104 ± 0.0374	1.7730	n.a.

[a] α = normalization factor, N = number of data point, and ϵ = systematic uncertainty. Data sets marked with an asterisk have not been used in the analysis because the evaluation of systematics is not available.

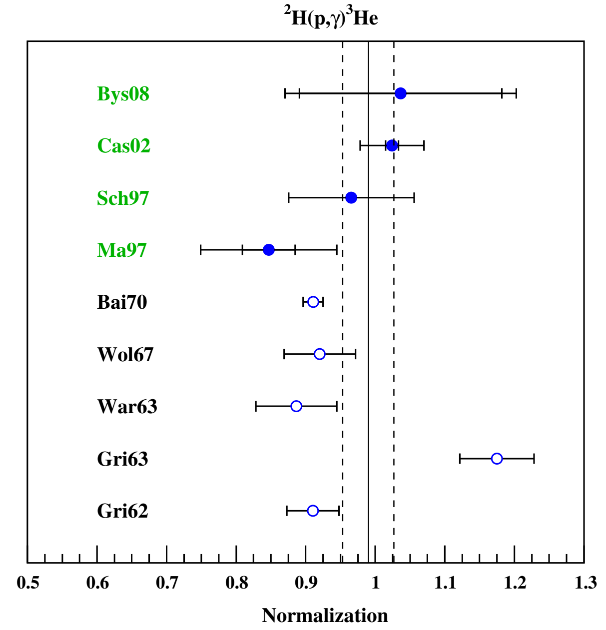

FIG. 2 (color online). Normalization factors (α) of the theoretical $d(p,\gamma)^3$He S factor for different experiments obtained by Eq. (A2) (blue circles). Full circles (green labels) correspond to data sets for which systematic uncertainties are available and are selected in the evaluation. Other data sets (open circles) are shown for comparison only and have not been used to derive our recommended average normalization factor. Their error bars correspond to uncertainties on the fit [Eq. (A3)] only. For the selected data sets (full circles) the error bars that include systematic uncertainties [Eq. (A8)] are superimposed. Vertical lines correspond to the average value [Eq. (A7)] and associated uncertainty [Eq. (A9)]. (References can be found in Table I.)

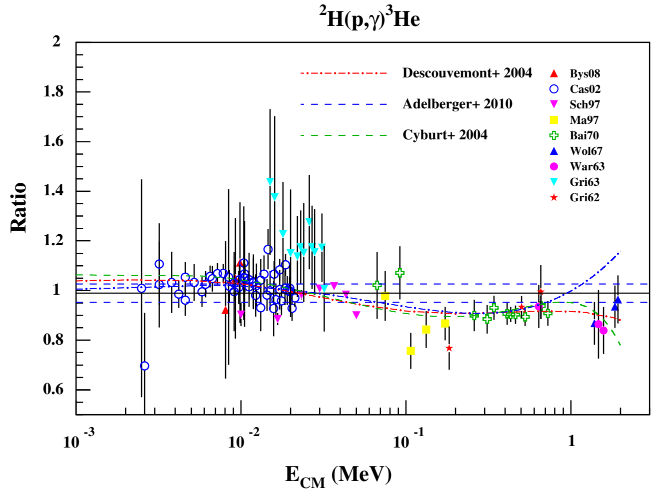

FIG. 3 (color online). Ratio of experimental and fitted S factors to the theoretical one [37]. The horizontal lines correspond to the theoretical S factor [37] normalized to a subset of the experimental data and the associated uncertainty (i.e., $\alpha \pm \Delta\alpha = 0.9900 \pm 0.0368$). Ratio of previous fits [13,15] are driven below theory by the scarce data at BBN energies.

with other evaluations, and *at BBN energies* our recommended S factor is higher. As a result, the BBN deuterium production calculated with our rate will be reduced (see Sec. V). Precise cross-section measurements at BBN energies (≈100 keV) are hence strongly needed.

III. THE D(d,n)^{3}He and D(d,p)^{3}H S FACTORS

The sensitivity of the D/H abundance ratio to $d(d,p)^3$H and $d(d,n)^3$He rate variations is [7]

$$\frac{\Delta(\mathrm{D/H})}{\mathrm{D/H}} = -0.54\frac{\Delta\langle\sigma v\rangle_{d(d,n)^3\mathrm{He}}}{\langle\sigma v\rangle_{d(d,n)^3\mathrm{He}}} - 0.46\frac{\Delta\langle\sigma v\rangle_{d(d,p)^3\mathrm{H}}}{\langle\sigma v\rangle_{d(d,p)^3\mathrm{H}}} \tag{3.1}$$

so that a precision of better than 2% is required for these rates.

Data from Refs. [40–43] were considered by the NACRE collaboration [20] and were also used in the R-matrix evaluation of DAACV [15]. Since DAACV, new measurements were performed by Leonard *et al.* [16] and by Tumino *et al.* [17]. Figures 4 and 5 display all the experimental data that we collected (see Appendix C). They show that the new, directly measured data [16] (labeled “Leo06” in figures) follow reasonably well the DAACV R-matrix fit, even though it was calculated before the experiment was conducted. These figures also display the results from an *ab initio* calculation by Arai *et al.* [44], which we normalize to the experimental data as described in Appendix A. This microscopic calculation uses a four-nucleon model with a realistic nucleon-nucleon interaction. It was shown that the tensor force plays an important role in the $d + d$ reactions. However, the theoretical work of Ref. [44] was focused on low energies, and only partial

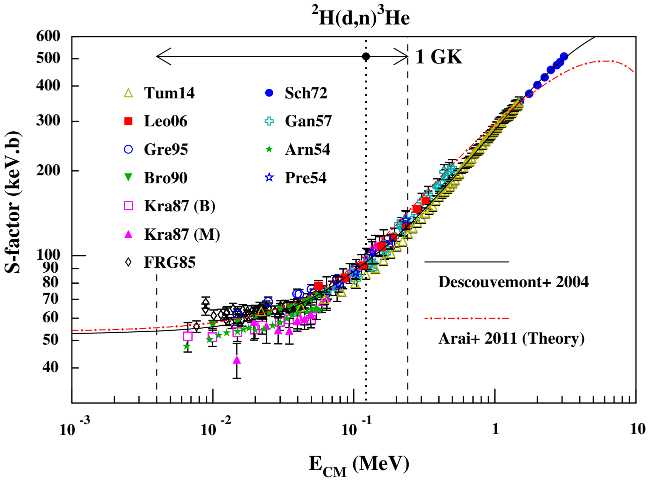

FIG. 4 (color online). Experimental data considered for $d(d,n)^3$He rate calculations, compared to DAACV R-matrix fit and theory [44]. The horizontal arrows indicate the Gamow window at 1 GK. (See references in Table II.)

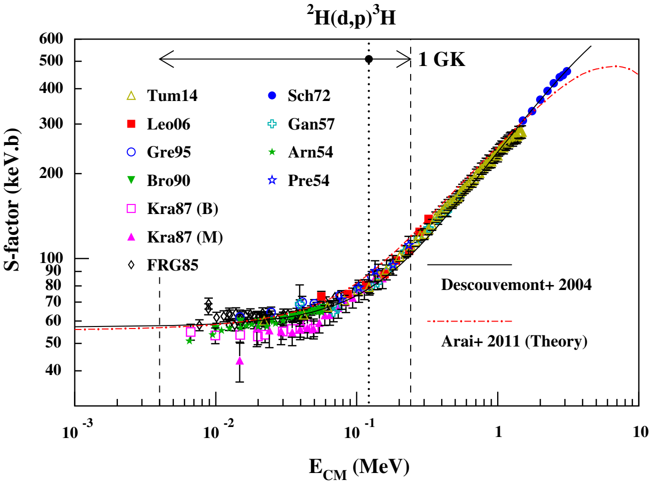

FIG. 5 (color online). Same as Fig. 4, but for $d(d,p)^3$H.

waves up to $J = 2$ have been included. For this reason, above 1 MeV, the theory underestimates the data. Consequently, we choose to limit the normalization to data below 0.6 MeV, which is well above the energy region important for BBN (dashed vertical lines).

Similar to our analysis of the $d(p,\gamma)^3$He reaction (Sec. II) we assume different normalization factors in different experiments and allow them to be different for $d(d,n)^3$He and $d(d,p)^3$H. The results of our fits for the collected 11 data sets [16,17,40–43,45–48] (Appendix C) can be found in Table II and in Figs. 6 and 7. Because of the limited energy range, 0.015 MeV $\leq E \leq$ 0.6 MeV (considering electron screening at low energy and nuclear model restrictions at high energy; see Appendix C), the number of adopted data points, N, is smaller compared to the original publications. For instance, because of these limitations, we had to disregard the data of Shulte *et al.* [40] and the lowest energy data of Krauss *et al.* [41].

In all experiments but one, we fitted the $d(d,n)^3$He and $d(d,p)^3$H data sets independently. Nevertheless, with a few exceptions, in a given experiment, the $d(d,n)^3$He (Fig. 6) and $d(d,p)^3$H (Fig. 7) normalization factors are very similar. For the data of Leonard *et al.* [16], we took advantage of the published error matrix and performed a fit taking into account all correlations between data points of different energies or reactions. This resulted in a simultaneous fit of both the $d(d,n)^3$He and the $d(d,p)^3$H cross sections. The results, displayed in Figs. 6 and 7 as grey squares show little difference with the simple fit (blue) circles and are not used. As for the $d(p,\gamma)^3$He reaction, we select the data sets for which the systematic uncertainties are published (see last column of Table II). As discussed in more detail in Appendix C, we do not use the indirect measurement from Tumino *et al.* [17] as the energy dependence of their experimental S factors is slightly different from theory and other experiments, in particular for the $d(d,n)^3$He reaction as it can be seen in Figs. 4 and 6.

For the recommended normalization factor, we obtain $\alpha = 0.9590 \pm 0.0104$ and $\alpha = 0.9549 \pm 0.0103$ (weighted average error) for the $d(d,n)^3$He and $d(d,p)^3$H reactions with reduced chi squares close to unity (1.33 and 0.92).

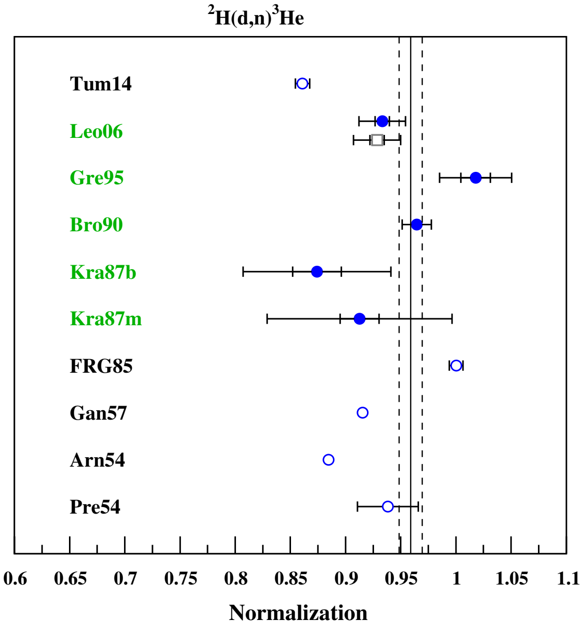

FIG. 6 (color online). Same as Fig. 2, but for the $d(d,n)^3$He reaction: only data shown by blue solid circles and green labels are used for the final normalization. Those selected data also display double error bars: the uncertainties from the fit and the total uncertainty including systematic uncertainties.

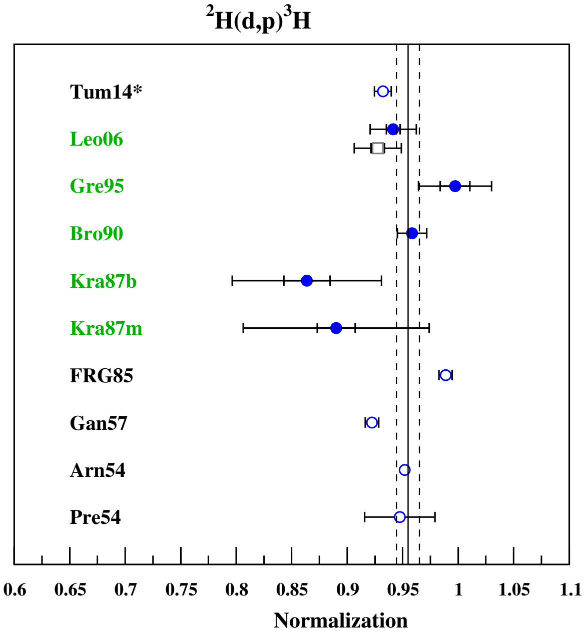

FIG. 7 (color online). Same as Fig. 2, but for the $d(d,p)^3$H reaction.

TABLE II. Results of normalization of individual data sets.

		$d(d,n)^3$He		$d(d,p)^3$H		
Reference	N	α	χ^2_ν	α	χ^2_ν	ϵ
Tum14* [17]	29	0.8610 ± 0.0064	1.0332	0.9322 ± 0.0075	0.1582	n.a.
Leo06 [16]	8	0.9333 ± 0.0065	2.0327	0.9415 ± 0.0061	5.3758	0.02
Gre95 [43]	8	1.0158 ± 0.0134	1.2472	0.9972 ± 0.0134	0.9989	0.03
Bro90 [42]	9	0.9644 ± 0.0025	2.3659	0.9584 ± 0.0020	1.9690	0.013
Kra87 (B) [41]	7	0.8683 ± 0.0220	0.2919	0.8637 ± 0.0208	0.1001	0.064
Kra87 (M) [41]	20	0.9185 ± 0.0177	0.6236	0.8902 ± 0.0171	0.1766	0.082
FRG85* [45]	45	0.9913 ± 0.0062	0.6509	0.9887 ± 0.0060	0.5044	n.a.
Gan57* [46]	36/18	0.9155 ± 0.0013	22.8927	0.9223 ± 0.0061	0.7350	n.a.
Arn54* [47]	15	0.8860 ± 0.0027	2.6995	0.9519 ± 0.0029	2.1919	n.a.
Pre54* [48]	5	0.9384 ± 0.0275	0.0988	0.9475 ± 0.0317	0.1186	n.a.

(We obtained similar results, $\alpha = 0.9579 \pm 0.0100$ and 0.9541 ± 0.0099, when using the alternative method presented in Appendix A 2.) Figures 8 and 9 display the scatter of all experimental data, in the $0.015\ \mathrm{MeV} \le E \le 0.6\ \mathrm{MeV}$ range, relative to the theoretical model from Ref. [44]. Data sets that significantly deviate from the fits were just not included in the fit (e.g., Tumino *et al.* [17] and Arnold *et al.* [47] for reasons discussed in Appendix C) or have large systematic uncertainties (Krauss *et al.* [41]) that are not included in the error bars of these figures.

IV. REACTION RATES AND UNCERTAINTIES

The reaction rates were calculated by numerical integration of the theoretical S factors, after normalization. Above the energies imposed by the limitations of the models [2 MeV and 0.6 MeV, respectively, for $d(p,\gamma)^3$He and $d+d$], the S factors are supplemented by the DAACV [15] results. The influence of this high energy S factor merging is negligible at BBN temperatures, but allows for calculating the tabulated rates on a conventional temperature grid. Figure 10 shows the new rates compared to the DAACV [15] that were used in previous works (e.g., Ref. [5]). In the upper panel [$d(p,\gamma)^3$He rate], we also display (dotted lines) the result of our numerical integration of the DAACV S factor within different energy intervals $E_0 \pm n\Delta E_0$, with $n = 2, 3, 4$, and 5, where E_0 and ΔE_0 define the Gamow window [e.g., Eqs. (5) and (6) in NACRE [20]]. In DAACV the rate was calculated with $n = 2$, not sufficient to reach the high precision needed here but that $n \gtrsim 3$ is required. Hence, to derive a more precise rate from our recommended S factors, we used a wider interval ($n = 4$) in our calculations. For each reaction, the 1σ uncertainties on rates, $N_A\langle\sigma v\rangle_{\mathrm{low}}^{\mathrm{high}}$, are obtained by using the 1σ uncertainties on the normalization factors ($\alpha \pm \Delta\alpha$) to rescale the theoretical S factors, or by using the DAACV uncertainty on the S factor at the highest energies. It is worth noting that these rate uncertainties are statistically defined (1σ limits), at variance with the limits provided in some other evaluations, e.g., NACRE [20] and NACRE-II [21]. The recommended reaction rates

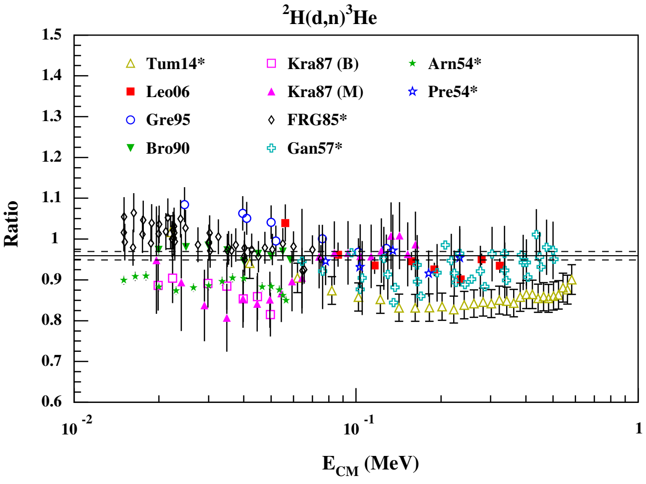

FIG. 8 (color online). Same as Fig. 3, but for the $d(d,n)^3$He reaction and $0.015\ \mathrm{MeV} \le E \le 0.6\ \mathrm{MeV}$.

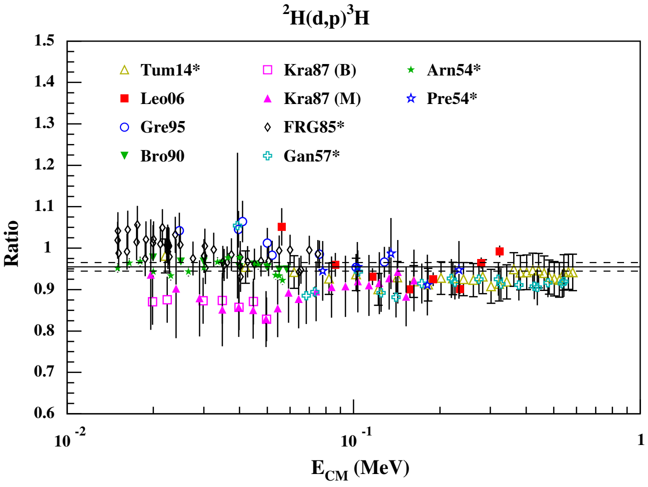

FIG. 9 (color online). Same as Fig. 3, but for the $d(d,p)^3$H reaction and $0.015\ \mathrm{MeV} \le E \le 0.6\ \mathrm{MeV}$.

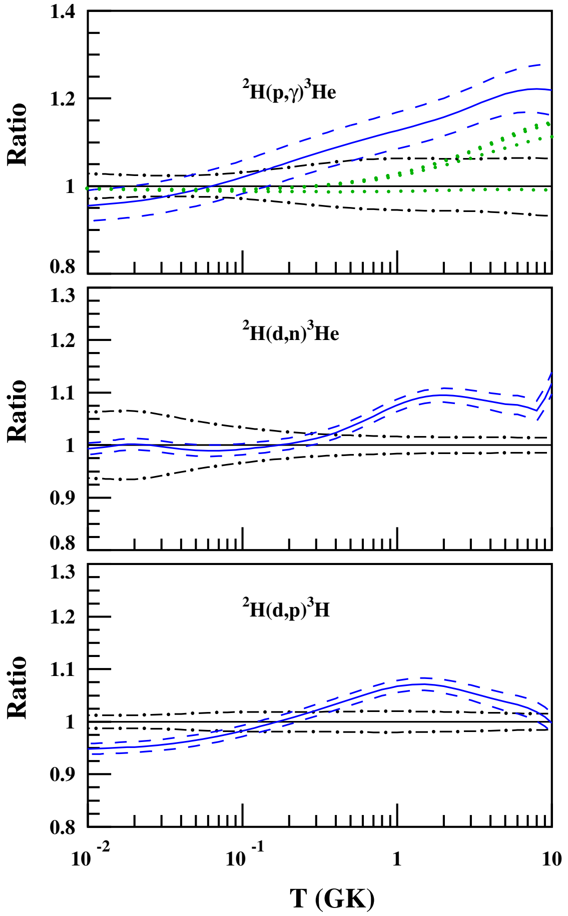

FIG. 10 (color online). New rates (blue curves), compared with previous [15] results (black curves), normalized to the DAACV [15] recommended rate. In the top panel, green curves: our recalculation of the $d(p,\gamma)^3$He reaction rate using the DAACV S factor, but with increased numerical integration limits.

$N_A\langle\sigma v\rangle_{\rm rec}$ calculated from the S factors rescaled by α can be found in Appendix D, together with the uncertainty factors, $(f.u.)$, defined [49] as

$$f.u. \equiv \sqrt{N_A\langle\sigma v\rangle_{\rm high}/N_A\langle\sigma v\rangle_{\rm low}}. \qquad (4.1)$$

Except at the highest energies where DAACV rate uncertainties are used, one simply has

$$f.u. = \sqrt{(\alpha+\Delta\alpha)/(\alpha-\Delta\alpha)} \approx 1 + \Delta\alpha/\alpha. \qquad (4.2)$$

In the Monte Carlo calculations, the reaction rates $N_A\langle\sigma v\rangle^k$ (with k being the index of the reaction), are assumed to follow a log-normal distribution,

$$N_A\langle\sigma v\rangle^k = \exp\left(\mu_k(T) + p_k\sigma_k(T)\right), \qquad (4.3)$$

where p_k is sampled according to a *normal* distribution of mean 0 and variance 1 [Eq. (4) of Ref. [50]]. The μ_k and σ_k determine the location of the distribution and its width. For the $d(p,\gamma)^3$He, $d(d,n)^3$He, and $d(d,p)^3$H reactions, they are derived from the values listed in Appendix D, using $\exp(\mu_k) \equiv N_A\langle\sigma v\rangle^k_{\rm rec}$ and $\exp(\sigma_k) \equiv (f.u.)^k$. From the resulting histograms of calculated abundances, the median and 68% confidence interval are obtained from the 0.5, 0.16, and 0.84 quantiles [49,50].

V. BBN RESULTS

The standard analysis of the CMB data by the Planck satellite showed that the temperature and polarization angular power spectra are consistent with a spatially Euclidean ΛCDM cosmological model with a power-law initial power spectrum for adiabatic scalar perturbations. The analysis includes parameters describing the baryonic and cold dark matter densities, the cosmological constant, the amplitude and spectral index of the primordial power spectrum, and the optical depth due to reionization. Besides, the present photon temperature is well measured to be $T_0 = 2.7255 \pm 0.0006$ K [51]. Assuming thermal equilibrium prior to neutrino decoupling, the radiation density is inferred by assuming that the effective number of neutrino families is $N_{\rm eff} = 3.046$ [52]. Among the various combinations of the temperature, E-polarization data, and lensing of the CMB by the large scale structure of the Universe (see Table 4 of Ref. [3]), we adopt the constraints obtained with the largest set of data (TT, TE, EE + lowP) without any external data and without taking the lensing data into account. This gives a constraint on the baryonic density parameter $\omega_{\rm b} = 0.02225 \pm 0.00016$ with a 68% confidence level.[3] In full generality, when combining data one should consider a consistent code predicting both the BBN abundances and the CMB angular power spectra. Note, in particular, that the latter requires us to determine the helium abundance that affects the recombination process since helium recombines before hydrogen. The Planck results [3] used a posterior mean of $Y_p \sim 0.2453$ "predicted by BBN, with theoretical uncertainties dominating over the Planck error $\Omega_{\rm b}h^2$…" (see Table 4 of Ref. [3]). One could introduce the new parameter Y_p but it is not free since it is related to $\omega_{\rm b}$ through BBN. The Planck analysis uses the PArthENoPE code [53] assuming a neutron mean lifetime of 880.3 s. Indeed, what is meant by "theoretical uncertainties" includes "uncertainties in the neutron lifetime and a few nuclear reaction rates." This emphasizes the importance of the present analysis that uses, compared to the PArthENoPE code, improved thermonuclear reaction rates relevant for D (and Li) nucleosynthesis. As a first analysis, and in order to confront Planck results with our BBN predictions, we compare the independent predictions of the CMB and BBN with 68% and

---

[3] This corresponds to a number of baryons per photon of $\eta = (6.0914 \pm 0.04380) \times 10^{-10}$, using $\eta = 2.7377 \times 10^{-8} \times \omega_{\rm b}$ [5].

TABLE III. Primordial abundances[a].

	a	b	c	d	e	f	*g (predicted)*	
ω_b	0.02218 ± 0.00026	0.02225	0.02225	0.02225	0.02225	0.02225	$\mathbf{0.02225 \pm 0.00016}$	h (observed)
Y_p	0.2482 ± 0.0003	0.2482	0.2482	0.2482	0.2484	0.2484	$\mathbf{0.2484 \pm 0.0002}$	0.2449 ± 0.0040 [4]
D/H ($\times 10^{-5}$)	$2.64^{+0.08}_{-0.07}$	2.635	2.635	2.635	2.526	2.452	$\mathbf{2.45 \pm 0.05}$	2.53 ± 0.04 [39]
^{3}He/H ($\times 10^{-5}$)	1.05 ± 0.03	1.047	1.047	1.047	1.038	1.070	$\mathbf{1.07 \pm 0.03}$	1.1 ± 0.2 [54]
^{7}Li/H ($\times 10^{-10}$)	$4.94^{+0.40}_{-0.38}$	5.040	5.102	5.131	5.343	5.651	$\mathbf{5.61 \pm 0.26}$	$1.58^{+0.35}_{-0.28}$ [55]

[a] Reference [5] (a); Updates of ω_b (b), $^7\mathrm{Be}(n,\alpha)^4\mathrm{He}$ (c), $^3\mathrm{He}(\alpha,\gamma)^7\mathrm{Be}$ (d), $d(d,n)^3\mathrm{He}$ and $d(d,p)^3\mathrm{H}$ (e), and $d(p,\gamma)^3\mathrm{He}$ (f) new rates, Monte Carlo (1σ) *(g)*, and observations (h).

95% confidence levels. Such a preliminary approach is sufficient to identify whether there is any tension between the two methods and to determine whether they are compatible at a given confidence level.

Table III shows the step by step progression of the ^{4}He, D, ^{3}He, and ^{7}Li abundances with improved input data (reaction rates and ω_b). The first column (a) lists the results of the Monte Carlo calculation from Ref. [5] (with $\omega_b = 0.02218 \pm 0.00026$ and for $\tau_n = 880.1 \pm 1.1$ s) for comparison. The second column (b) uses the same 425-reaction network but for $\omega_b = 0.02225$ (and $\tau_n = 880.3$ s). The largest difference, on ^{7}Li, between the median of the Monte Carlo distribution of abundances (a) and the calculation using nominal values of parameters (b), is due to the non-Gaussian shape of the Li/H abundance distribution, to statistical fluctuations, and to minute updates of physical constants. Two rates affecting ^{7}Be nucleosynthesis have been updated since DAACV [15]. The $^3\mathrm{He}(\alpha,\gamma)^7\mathrm{Be}$ rate from DAACV had been superseded by Cyburt and Davids [56], who included new results from LUNA. An improved evaluation of the $^3\mathrm{He}(\alpha,\gamma)^7\mathrm{Be}$ reaction rate and associated uncertainty has been published [57] since, using a Monte Carlo based *R*-matrix analysis, and can be considered up to date. Even though the $^7\mathrm{Be}(n,\alpha)^4\mathrm{He}$ reaction cannot help solve the lithium problem, its rate was uncertain and affected the ^{7}Li production at the few percent level. Until recently, the only published rate came from an evaluation by Wagoner [58]. Very recently, Hou *et al.* [59] clarified the origin of the Wagoner rate, but more importantly have reevaluated it, based on $^4\mathrm{He}(\alpha,n)^7\mathrm{Be}$, $^4\mathrm{He}(\alpha,p)^7\mathrm{Li}$, and $^7\mathrm{Li}(p,\alpha)^4\mathrm{He}$ experimental data, using charge symmetry and/or detailed balance principles. The next two columns, (c) and (d), in Table III show the effect of updating the $^7\mathrm{Be}(n,\alpha)^4\mathrm{He}$ [59] and $^3\mathrm{He}(\alpha,\gamma)^7\mathrm{Be}$ [57] rates, respectively. The effects of using our new $d(d,n)^3\mathrm{He}$ and $d(d,p)^3\mathrm{H}$ and $d(p,\gamma)^3\mathrm{He}$ rates instead of DAACV [15] are displayed in the next columns, (e) and (f), respectively. As expected from Fig. 10, the D/H abundance is significantly reduced, together with a concomitant ^{7}Li increase. The results of a Monte Carlo calculation, performed as in Ref. [5], but with the updated rates and $\omega_b = 0.02225 \pm 0.00016$ [3] (see above) and $\tau_n = 880.3 \pm 1.1$ s [60] are shown in column (g), compared to observations (h). For deuterium, we obtain

$$\mathrm{D/H} = (2.45 \pm 0.10) \times 10^{-5} (2\sigma). \qquad (5.1)$$

VI. COSMIC DEUTERIUM EVOLUTION

Starting from our new BBN prediction [Eq. (5.1)], it is interesting to follow the cosmic deuterium evolution. This isotope is a good tracer of stellar formation since it can be destroyed only after the BBN stage.

A. Observations

The primitive abundance of deuterium is determined from the observation of cosmological clouds at high redshift located on the line of sight of distant quasars. Very few observations are available so far. Pettini and Cooke [61] and, more recently, Cooke *et al.* [39] observed, or reanalyzed, five DLA systems at redshift 2–3 and derived a mean value $\mathrm{D/H} = (2.53 \pm 0.04) \times 10^{-5}$. Recently, Riemer-Sørensen *et al.* [62] remeasured the $z = 3.256$ absorption system toward the quasar PKS 1937 − 101 and have determined a robust value of $\mathrm{D/H} = (2.45 \pm 0.28) \times 10^{-5}$. Finally Noterdaeme *et al.* [63] measured $\mathrm{D/H} = (2.59 \pm 0.15) \times 10^{-5}$ at $z = 2.621$ toward CTQ 247. Our present BBN D/H calculated value of $(2.45 \pm 0.10) \times 10^{-5}$ (2σ) is in agreement with these observational constraints, although the observations tend to be slightly higher.

The D/H ratio can also be derived from observations of HD and $\mathrm{H_2}$ molecules in DLAs assuming that chemistry does not affect its value. The observed ratios take very different values, which may cast some doubt on this latter assumption [64]. Srianand *et al.* [65], Ivanchik *et al.* [66], and Balashev *et al.* [67] measured $\mathrm{D/H} = (1.17^{+0.49}_{-0.34}) \times 10^{-5}$, $(3.6^{+1.9}_{-1.1}) \times 10^{-5}$, and $(3.6^{+1.9}_{-1.1}) \times 10^{-5}$ toward J1337 + 3152, Q 1232 + 082, and both J 0812 + 3208 and Q 1331 + 170 at $z = 3.102$, 2.3377, and 2.626 and 1.777, respectively. Indeed, Le Petit *et al.* [68] modeled the deuterium chemistry and showed that the derived D/H ratio strongly depends on the initial physical conditions such as temperature and density. However, they considered dense clouds, whereas most DLAs are diffuse structures. Since the situation is not clear, it is premature to use these observational measurements to compare with the results of our models.

Recent local D/H observations added new constraints on the cosmic deuterium astration factor, f_D, which is defined as the ratio of the BBN to the present deuterium abundances, $\mathrm{D_{BBN}/D_{present}}$. In the local interstellar medium (ISM), Prodanović *et al.* [69] find their best estimate for the undepleted ISM deuterium abundance to be $\mathrm{D/H} = (2.0 \pm 0.1) \times 10^{-5}$, leading to $f_D < 1.26 \pm 0.1$. In the local galactic disk, Linsky *et al.* [70] analyzed spectra obtained with the Far Ultraviolet Spectroscopic Explorer (FUSE) satellite, together with spectra from the Copernicus and interstellar medium absorption profile spectrograph (IMAPS) instruments. This study reveals a very wide range in the observed D/H ratio. Spatial variations in the depletion of deuterium in dust grains could explain these local variations. Finally, they argue that the most representative value for the D/H ratio within 1 kpc of the Sun is $(2.31 \pm 0.24) \times 10^{-5}$. The deuterium astration factor, f_D, is in this context less than 1.1. Finally, Savage *et al.* [71] use high-resolution ultraviolet spectra in the lower galactic halo and obtain $\mathrm{D/H} = (2.2^{+0.8}_{-0.6}) \times 10^{-5}$. This value is consistent with the results mentioned above, but with a very large error bar.

B. Evolution

We now consider the cosmic evolution of D/H in a cosmological context in the light of the new, somewhat low, deuterium primordial value derived here. It is well known that, due to its fragility, deuterium is destroyed during the cosmic evolution (as soon as $T > 10^5$ K). In this context, we follow the cosmic chemical evolution using a model developed in Refs. [72–74], based on a hierarchical model for structure formation [75,76]. A key ingredient to all evolution models is the global cosmic star formation rate (SFR; a specific analysis devoted to different SFRs is performed in Ref. [74]), whose evolution with redshift is constrained by many observations. Recent data from high redshift galaxy observations (the Hubble Ultra Deep Field) have significantly extended the range of redshifts for its determination, from $z = 4$ up to 10 [77,78]. Figure 11 shows the SFR fit using these observations (blue points and blue dotted line). On the other hand, observations of high z gamma-ray bursts (GRBs) tend to favor a large amount of yet unobserved SFR at $z > 9$ [82] (black points and black solid line). Extracting the SFR from the GRB rate is not free from uncertainties and biases [79]. In the following, we will use the SFR derived from Ref. [79] (see Figure 11, black line), which is consistent with other observational constraints as shown by Vangioni *et al.* [74]. To estimate the maximum astration factor of D, we have also considered an extreme case, adding an intermediate mass SFR component (between 2 and 8 $M_\odot$), which is shown in Fig. 11 by the black dashed curve. Note that the exact slope of the SFR at high redshift has no impact on the deuterium evolution (contrary to heavier elements). Indeed, it is well known that deuterium destruction is governed by low mass stars (since the gas is essentially trapped in these stars), whereas metallicity production (elements other than H and He) is governed by high mass stars, which, having short lifetimes, start rejection of enriched matter at high redshift. A weak destruction of deuterium is consequently not incompatible with a significant formation of heavy elements.

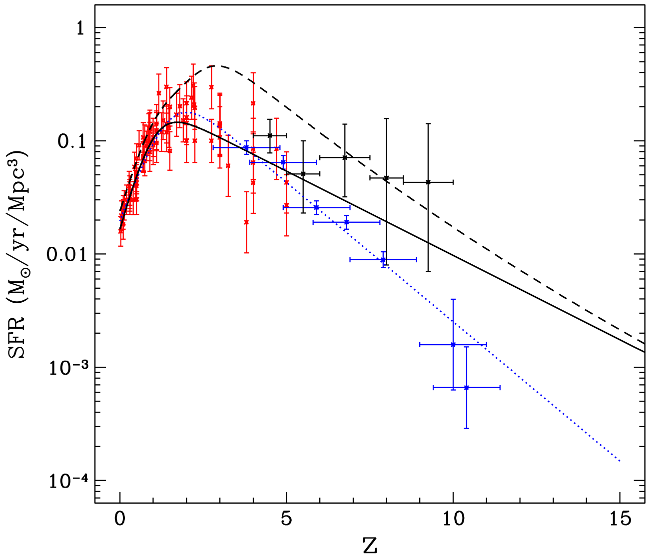

FIG. 11 (color online). Cosmic SFR as a function of redshift. The solid black line fit from Trenti *et al.* [79] and Behroozi and Silk [80] (see also Vangioni *et al.* [74]) is adopted in the present work. The dashed black curve corresponds to an upper limit of the SFR, an extreme case obtained by adding an intermediate mass SFR component (between 2 and 8 $M_\odot$) to maximize the deuterium destruction. For comparison, the dotted blue line fits the observations coming from high redshift galaxy surveys [81] (red points) and [77,78] (and references therein) (blue points). The exact slope of the SFR at high redshift has little impact on the deuterium evolution.

Assuming a given cosmic evolution of the SFR, the model follows the evolution of the baryons abundance in stars, in diffuse structures [interstellar medium (ISM)], and in the intergalactic medium (IGM). The model includes a description of mass exchanges between the IGM and ISM (structure formation, galactic outflows), and between the ISM and the stellar component (star formation, stellar winds, and supernova explosions). Once the cosmic SFR is specified, several quantities are obtained as a function of the redshift, namely the abundances of chemical elements, and more specifically deuterium. We consider for the present study the results of the best model described in Ref. [74], including a standard mode of Population II/I star formation between $0.1\,M_\odot$ and $100\,M_\odot$. The initial mass function (IMF) slope is set to the Salpeter value, i.e., $x = 1.35$ [83,84].

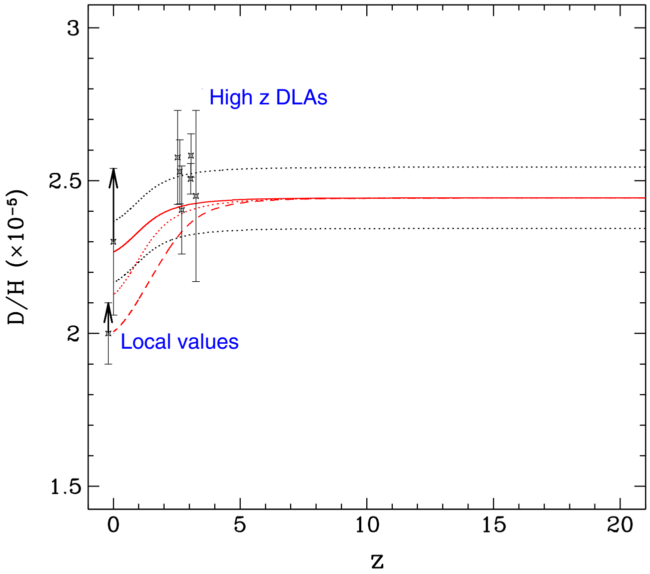

FIG. 12 (color online). Cosmic deuterium evolution as a function of redshift. The deuterium evolution using the SFR shown in Fig. 11. The red solid curve corresponds to the evolution of D/H using our mean BBN value, whereas the black dotted curves correspond to the higher and lower (2σ) limits. High z DLAs observations come from Cooke *et al.* [39] and Riemer-Sørensen *et al.* [62], whereas local observations come from Linsky *et al.* [70] and Prodanović *et al.* [69]. The lower mass of the IMF is taken here as $0.1\,M_\odot$. Regarding the sensitivity to the IMF parameters, we show the impact of having a different lower mass of the IMF ($0.5\,M_\odot$, dotted red line) or adding an intermediate mass formation (between 2 and $8\,M_\odot$, dashed red line).

Figure 12 shows the evolution of D/H as a function of redshift, derived with the cosmic SFR shown in Fig. 11 (solid black line). Black dotted curves correspond to our 2σ BBN limits, whereas the red solid line corresponds to the mean. The resulting astration factor is $f_D = 1.1$. This cosmic evolution is in overall agreement with the observed values detailed above. Note, however, that a tension exists between the BBN value and the high redshift measurements in the sense that the latter seem somewhat high. However, note that, owing to the extreme fragility of deuterium, its potential destruction depends on many parameters of the star-formation history and, in particular, the IMF parameters. We illustrate the impact of the variation of the mass lower limit of the IMF. The dotted red curve corresponds to a lower mass limit of $0.5\,M_\odot$ instead of $0.1\,M_\odot$ (solid red line). In this case the astration factor is $f_D = 1.15$. Finally, we consider an extreme case by adding an intermediate mass star formation component (between 2 and $8\,M_\odot$) (dashed red line), leading to an astration factor of $f_D = 1.25$. Even when considering these extreme modifications of the IMF, the maximum variation is only 14%, which is not a large uncertainty compared to the error bars on observational data. Recently, Prodanović, Steigman, and Fields [85] have studied the deuterium evolution and its link with structure formation. They show that a steady infall rate is required to reconcile the model with observations. Our cosmological model is in agreement with this result since in a hierarchical formation of structures, primordial gas is continuously accreted into structures throughout the evolution. We also find, as did these authors, that 80% of the initial interstellar gas is never processed within stars.

Since the paper is devoted to deuterium study we do not consider other elements. Obviously, deuterium destruction can lead to ^{3}He production, but while we have D/H cosmological observations, we have only ^{3}He/H local observations (in the galactic disk) and no constraints at high redshift. Chiappini *et al.* [86] and Vangioni-Flam *et al.* [87] have analyzed the behavior of ^{3}He in the Galaxy. The best observational constraints come from Bania *et al.* [54]. These data are concentrated in the galactic disk only, i.e., at high metallicity relative to the solar value ([O/H] between -0.6 and 0.2). Vangioni-Flam *et al.* have shown that it is not possible to obtain a strong constraint on the baryon density using ^{3}He due to this limited range of metallicity in the sample and to the limited understanding of the chemical and stellar evolution of this isotope.

To conclude, our results are in agreement with the observations, implying that the mean abundance of deuterium has only been reduced by a factor of 1.1 to 1.25 since its formation during BBN. There is, however, a tension between our BBN D/H value and the high-z measurements, leaving little room for a high astration factor. In any case, due to the low abundance of the primordial D/H value and the local observed constraints, the astration factor, f_D, is less than 1.25.

VII. THE LITHIUM-DEUTERIUM ANTICORRELATION

In spite of various efforts, there is still a factor of ≈3.5 (Table III) between the predicted and observed lithium primordial abundances. Most proposed solutions to the lithium problem lead to an increase of the deuterium production [10,88,89]; they are now strongly constrained by deuterium observations. We discuss here the relation between lithium (^{7}Be + ^{7}Li) destruction and D overproduction.

At CMB deduced baryonic density, ^{7}Li is produced indirectly by $^3\mathrm{He}(\alpha,\gamma)^7\mathrm{Be}$, where ^{7}Be will much later decay to ^{7}Li, while ^{7}Be is destroyed by $^7\mathrm{Be}(n,p)^7\mathrm{Li}(p,\alpha)^4\mathrm{He}$. The solutions to the lithium problem generally rely on an increased late time neutron abundance [90–92] to boost ^{7}Be destruction through the $^7\mathrm{Be}(n,p)^7\mathrm{Li}(p,\alpha)^4\mathrm{He}$ channel. These extra neutrons, inevitably, also boost the D and ^{3}H production through the $^1\mathrm{H}(n,\gamma)^2\mathrm{H}$ and $^3\mathrm{He}(n,p)^3\mathrm{H}$ channels, respectively [89]. For instance, Fig. 13 displays the effect of the injection of thermalized neutrons at a constant rate (as in Albornoz Vásquez *et al.* [92]).

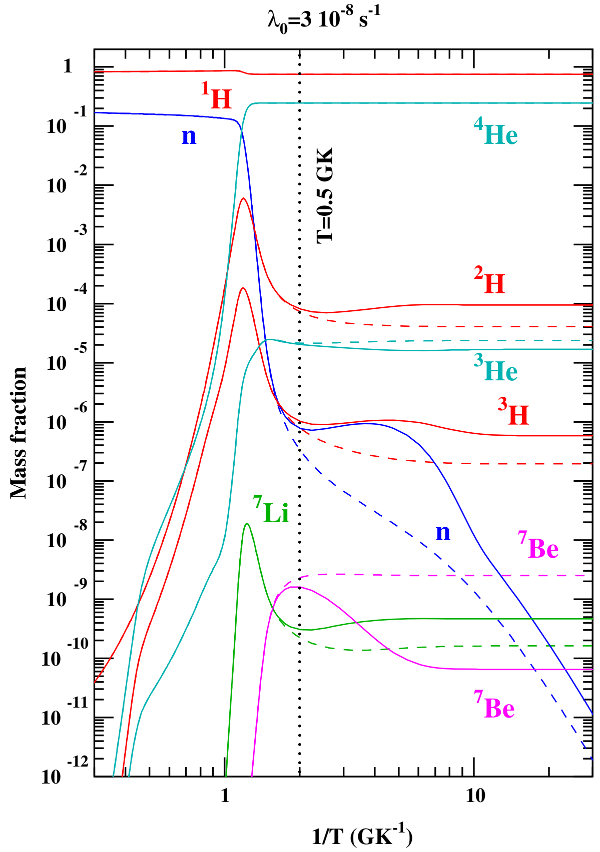

FIG. 13 (color online). Effect of thermal neutron injection, at a rate of $\lambda_0 = 3 \times 10^{-8}$ s^{-1}, on abundances (solid lines) as functions of the inverse of temperature ($1/T$), compared to the standard calculation (dashed lines): ^{7}Be and ^{3}He abundances decrease, while ^{7}Li and ^{3}H abundances increase. Note the crossing of ^{7}Li and ^{7}Be abundance curves.

Even though other destruction channels by other thermalized[4] particles (p, d, t, ^{3}He, and α) have been investigated [94], neutron capture remains the only efficient one. Neutron induced reaction rates vary far less with temperature compared to charged-particle induced reaction rates at BBN temperatures. For instance, a factor of $\sim 3 \times 10^{-5}$ for the $^7\mathrm{Be}(p,\gamma)^8\mathrm{B}$ is to be compared to a factor of 2 for the $^7\mathrm{Be}(n,p)^7\mathrm{Li}$ reaction, when the temperature drops from 1.0 to 0.1 GK. This is obviously directly linked to Coulomb barrier penetration. After ≈700 s, when the ^{7}Be abundance has reached its maximum (Fig. 13), the temperature is lower than 0.5 GK. This low temperature prevents charged particle reactions from being efficient, as it can be seen in Fig. 13 by the flat (dashed lines) final evolution of the abundances. [In any case, the $^7\mathrm{Be}(p,\gamma)^8\mathrm{B}$ reaction has such a low Q value (0.1375 MeV) that the reverse reaction, photodisintegration, is so effective that it prevents ^{7}Be destruction by proton capture.] This could only be circumvented by the presence of strong resonances in some charged particle induced reactions, like $^7\mathrm{Be}(d,p)2\alpha$. However, experiments have not supported such a nuclear physics solution involving new conventional neutron sources [95] or new resonances [12,96] in reactions with a charged particle, suggesting nonconventional neutron sources as a solution.

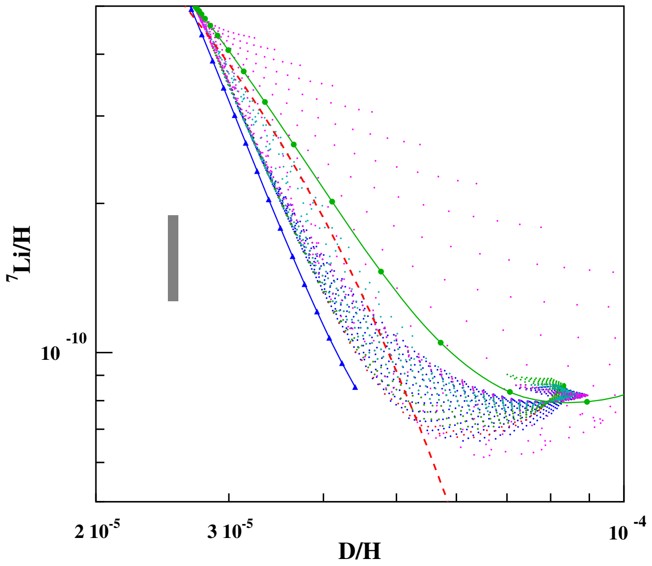

FIG. 14 (color online). Lithium-deuterium anticorrelation in BBN induced by different models involving neutron injection (dots: update of Fig. 9 in Ref. [10]; green circles: Fig. 7 in Ref. [10]; and blue triangles, Fig. 12 in Ref. [97]). The grey box represents the observational constraints [39,55], while the dashed line [Eq. (7.4)] is a qualitative explanation of the anticorrelation.

Figure 14 is adapted from Fig. 9 in Ref. [10] summarizing the results of different models that include late time neutron injection aiming at reducing the $^7\mathrm{Be} + {}^7\mathrm{Li}$ production, but at the expense of D overproduction. These models involve mirror neutrons, dark matter decay, or annihilation as extra neutron sources. The figure also displays the results of a BBN calculation allowing for a coupled variation of constants as described in Ref. [97], where the extra neutron source arises from the change induced in the $^1\mathrm{H}(n,\gamma)^2\mathrm{H}$ rate.

Figure 13 shows that ^{7}Be increased destruction by neutrons is counterbalanced by ^{7}Li increased production. First, with a higher ^{3}H abundance, owing to the $^3\mathrm{He}(n,p)^3\mathrm{H}$ increased efficiency, the $^3\mathrm{H}(\alpha,\gamma)^7\mathrm{Li}$ channel, normally negligible at η_{CMB}, may become dominant. Second, the ^{7}Be increased destruction by $^7\mathrm{Be}(n,p)^7\mathrm{Li}$, produces ^{7}Li that is not efficiently destroyed anymore by $^7\mathrm{Li}(p,\alpha)^4\mathrm{He}$, because of the low temperature. This explains that when increasing the rate of injection of extra neutrons, the $\mathrm{Li} = {}^7\mathrm{Be} + {}^7\mathrm{Li}$ abundance reaches a minimum as seen in Fig. 14 (or in Fig. 7 of Ref. [10]). This lower limit on Li/H, owing to the transition from ^{7}Be to ^{7}Li direct production (Figs. 13 and 14), can be compared to the minimum in Li/H as a function of η.

---

[4] As opposed to nonthermalized particles originating from the decay of massive relic particles during BBN (see, e.g., Ref. [93]).

Figure 13 also shows that the effect of ^{7}Be destruction by extra neutrons is efficient only below ≈0.5 GK when the charged particle reactions are inefficient due to the Coulomb barrier and the low abundance of reactants. If we call $\delta Y_{\mathrm{n}}(t)$ the extra, late time, neutron overabundance, the extra destruction of ^{7}Be is given by

$$\frac{\mathrm{d}Y_{^7\mathrm{Be}}}{\mathrm{d}t} = -Y_{^7\mathrm{Be}}\rho N_A\langle\sigma v\rangle_{\mathrm{be7np}}\delta Y_{\mathrm{n}}, \qquad (7.1)$$

where $Y(t)$ are mole fractions, $\rho(t)$ the baryonic density, and $N_A\langle\sigma v\rangle$ the thermonuclear reaction rate. We neglect the $^3\mathrm{He}(\alpha,\gamma)^7\mathrm{Be}$ channel at those low temperatures because of the Coulomb barrier (Fig. 13).

At the same time, an extra deuterium production from the $n(p,\gamma)d$ reaction *is unavoidable*, so that

$$\frac{\mathrm{d}Y_{\mathrm{D}}}{\mathrm{d}t} = +Y_{\mathrm{H}}\rho N_A\langle\sigma v\rangle_{pn\gamma}\delta Y_n. \qquad (7.2)$$

Again, we neglect charged particle reactions and the $^3\mathrm{He}(n,p)^3\mathrm{H}$ neutron drain, as we do not need to calculate $\delta Y_{\mathrm{n}}(t)$. Putting Eqs. (7.1) and (7.2) together, one obtains

$$\mathrm{d}\ \ln\left(\frac{Y_{^7\mathrm{Be}}}{Y_{\mathrm{H}}}\right) = -\left[\frac{\langle\sigma v\rangle_{\mathrm{Be}7np}}{\langle\sigma v\rangle_{pn\gamma}}\right]\mathrm{d}\left(\frac{Y_{\mathrm{D}}}{Y_{\mathrm{H}}}\right). \qquad (7.3)$$

Since, the ratio of $^7\mathrm{Be}(n,p)^7\mathrm{Li}$ to $^1\mathrm{H}(n,\gamma)^2\mathrm{H}$ thermonuclear reaction rates is almost constant [$(6\text{–}8)\times 10^4$ for $0.1 < T < 1$ GK], one can deduce that

$$\frac{\mathrm{D}}{\mathrm{H}} \approx \left.\frac{\mathrm{D}}{\mathrm{H}}\right|_0 - \left[\ln\left(\frac{\mathrm{Li}}{\mathrm{H}}\right) - \ln\left.\left(\frac{\mathrm{Li}}{\mathrm{H}}\right)\right|_0\right] \times 1.4\times 10^{-5}, \qquad (7.4)$$

which is displayed (red dashed line) in Fig. 14. This is an approximation, as long as $Y_{^7\mathrm{Li}} \ll Y_{^7\mathrm{Be}}$, but it gives a qualitative explanation for the lithium-deuterium anticorrelation in most models aiming at solving the lithium overproduction. Depending on the precise timing of neutron injection, and hence, of the temperature, the efficiency of neglected reactions [e.g., $d+d$ and $^7\mathrm{Li}(p,\alpha)^4\mathrm{He}$] need to be considered [89], but this would increase the complexity of the calculations. Here, we only considered thermalized neutron injection, first, because thermalization of high energy neutrons is fast [92]. Second, it was already noted by Kusakabe *et al.* [89] that the ratio of $^1\mathrm{H}+n$ to $^7\mathrm{Be}+n$ cross sections increases with energy, rendering less efficient the injection of nonthermalized neutrons for destroying ^{7}Be without overproducing deuterium, when compared with thermal neutron injection.

VIII. CONCLUSIONS

It has long been recognized that the agreement between BBN predictions and observations is quite satisfactory except for lithium. Now that the observations of D/H in cosmological clouds, thought to be representative of the primordial abundance, have reached a high precision [39], nuclear cross sections of all reactions leading to deuterium destruction should be determined with an equivalent precision [19], i.e., at the percent level. To improve the precision on the three main reaction rates governing deuterium destruction, we have reevaluated existing experimental data, using S factors provided by *ab initio* theoretical models. This is at variance with most other reaction rate evaluations that rely on phenomenological approaches (e.g., polynomial or R matrix) fits of experimental data. We paid special attention to systematic uncertainties in the selection of the data sets to be considered. In particular, for the $d(d,n)^3\mathrm{He}$ and $d(d,p)^3\mathrm{H}$ S factors, we take advantage of the mostly model independent ratio of cross sections to evaluate experimental results. The three reaction rates are found to be slightly higher than the previous R-matrix analysis of DAACV [15], leading to a small but significant decrease of the D/H prediction, $(2.45\pm 0.05)\times 10^{-5}$. We calculate the cosmological evolution of deuterium from BBN until the present, within a hierarchical model of structure formation and obtained a value of D/H = $(2.42\pm 0.05)\times 10^{-5}$, at the redshift ($z\approx 3.0$) of the observed cosmological clouds. This predicted value is compatible at the 2σ level with the observations $(2.53\pm 0.04)\times 10^{-5}$ [39].

Deuterium predictions are also highly important, in relation with the lithium problem. Most solutions involve a ^{7}Be destruction by a late time neutron injection. We show that this is unavoidably correlated with an increase of the deuterium production by the effect of the $^1\mathrm{H}(n,\gamma)^2\mathrm{H}$ reaction. Hence, most solutions to the lithium problem are now severely constrained, also by deuterium precise observations.

Further progress in the domain is expected from future experiments, in particular, concerning the $d(p,\gamma)^3\mathrm{He}$ reaction, planned to be measured at the BBN energies, at the Gran Sasso National Laboratory (LUNA), but also, possibly, from improved theory.[5] Keeping systematic uncertainties on nuclear cross-section measurements at the percent level is indeed a challenge. These systematics can be evaluated by comparing independent measurements, with the help of theoretical S factors when data sets span different energy ranges.

ACKNOWLEDGMENTS

This work done in the ILP LABEX (under Grant No. ANR-10-LABX-63) was supported by French state funds managed by the ANR within the Investissements

---

[5] A very recent, improved *ab initio* calculation of the $d(p,\gamma)^3\mathrm{He}$ S factor [98] has led to a reduced D/H prediction of $(2.49\pm 0.03\pm 0.03)\times 10^{-5}$ compared to the previous value of $(2.61\pm 0.14)\times 10^{-5}$ [3].

d'Avenir programme under Grant No. ANR-11-IDEX-0004-02 and by the ANR VACOUL, Grant No. ANR-10-BLAN-0510.

APPENDIX A: NORMALIZATION PROCEDURE

In other evaluations [13,15,20], the S-factor shapes (polynomial, R matrix) were fitted on experimental data. Here, we assume that theory $[F(E)]$ gives a good description of the shape but may need a scaling factor α (i.e., $F \to \alpha F$). Calculations involve an energy dependence and an overall normalization. The energy dependence is essentially provided by the Coulomb functions and is therefore more reliable than the normalization, which is more sensitive to the model assumptions. Accordingly, we introduce a possible scaling of the theoretical calculations with a renormalization factor α_k, close to unity. By minimizing the χ^2,

$$\chi^2(\alpha_k) = \sum_{i_k} \frac{[S(E_{i_k}) - \alpha_k F(E_{i_k})]^2}{\sigma^2_{i_k}}, \tag{A1}$$

where $S(E_{i_k})$ and σ_{i_k} are the experimental S factors and associated uncertainties, one obtains the scale factor best value ($\hat{\alpha}_k$) and associated uncertainty ($\sigma_{\hat{\alpha};k}$) (for a given experiment labeled k for future use) that are given by Eqs. (A2) and (A3) [Eqs. (6) and (7) in [99]]

$$\hat{\alpha}_k = \frac{\sum_i S(E_{i_k}) F(E_{i_k})/\sigma^2_{i_k}}{\sum_{i_k} F^2(E_{i_k})/\sigma^2_{i_k}}, \tag{A2}$$

$$\sigma_{\hat{\alpha};k} = \frac{1}{\sqrt{\sum_{i_k} F^2(E_{i_k})/\sigma^2_{i_k}}}. \tag{A3}$$

This takes well into account the effect of statistical uncertainties but leaves aside systematic uncertainties, in particular on the normalization. Systematics coming from different normalizations, from one data set to the other, will play an essential role. It is usually recommended [60], for incompatible data sets, to inflate the classical error [Eq. (A3)], by a factor of $\sqrt{\chi^2_\nu}$ so that the final reduced χ^2 equals 1 ($\sqrt{\chi^2_\nu} = 1$). This method has, however, been questioned. We present in this section several options that have been considered, apply them to experimental data sets in the following sections, and compare the results.

1. The global data fit option

Cyburt *et al.* [99] used this procedure to renormalize the NACRE S-factor fits, and this is identical to our goal except that we use the theoretical S factor instead.

The value of the normalization factor, α, is again given by Eq. (A2) [their Eq. (6)], except that now the sum runs over all the data points ($i_k = 1 \cdots N_k$) within all the N data sets,

$$\hat{\alpha} = \frac{\sum_{k=1}^{N} \sum_{i_k=1}^{N_k} S_k(E_{i_k}) F(E_{i_k})/\sigma^2_{i_k}}{\sum_{k=1}^{N} \sum_{i_k=1}^{N_k} F^2(E_{i_k})/\sigma^2_{i_k}}. \tag{A4}$$

But the σ_α value proposed by Cyburt *et al.* [99] is now given by their Eq. (11) instead of their Eq. (7) [our Eq. (A3)],

$$\sigma^2_{\hat{\alpha}} = \frac{\sum_{k=1}^{N} \sum_{i_k=1}^{N_k} [S_k(E_{i_k}) - \hat{\alpha} F(E_{i_k})]^2/\sigma^2_{i_k}}{\sum_{k=1}^{N} \sum_{i_k=1}^{N_k} \hat{\alpha}^2 F^2(E_{i_k})/\sigma^2_{i_k}}. \tag{A5}$$

We note that it corresponds to Eq. (A3) (with $F \to \hat{\alpha} F$), i.e., the classical error, but is inflated by $\sqrt{\chi^2}$ instead of $\sqrt{\chi^2_\nu}$ as it is usually recommended for incompatible data sets [60].

2. The joint statistical and normalization fit option

The method from D'Agostini [100] has been used, in particular, by Serpico *et al.* [14] for BBN reaction rate evaluations, and by Cyburt and Davids [56] and Schürmann *et al.* [101] for the $^3\mathrm{He}(\alpha,\gamma)^7\mathrm{Be}$ and $^{12}\mathrm{C}(\alpha,\gamma)^{16}\mathrm{C}$ reactions, respectively. In addition to the parameters of the theoretical model (a single one, α, in our case), scale factors, ω_k, with associated errors, ϵ_k, affect all data sets. Note that the ϵ_k, for each experiment, are not always available. In that case, Serpico *et al.* [14] write, "Whenever only a total error $\sigma^{\mathrm{tot}}_{i_k}$ determination is available for a certain experiment, that error is used instead of σ_{i_k}, and an upper limit on the scale error is estimated as $\max[\sigma^{\mathrm{tot}}_{i_k}/Si_{i_k}]$." The χ^2 to be minimized has the form

$$\chi^2(\alpha, \boldsymbol{\omega}) = \sum_{k=1}^{N} \left(\sum_{i_k=1}^{N_k} \frac{[\omega_k S(E_{i_k}) - \alpha F(E_{i_k})]^2}{\omega_k^2 \sigma^2_{i_k}} + \frac{(\omega_k - 1)^2}{\epsilon_k^2} \right). \tag{A6}$$

Hence, the experimental values are scaled by factors that are constrained by the experimental uncertainty on normalization while the theoretical function is also scaled by the factor we want to determine. The minimization procedure is no longer trivial, and we have to perform it numerically with the use of MINUIT [102]. It is no longer possible to give an analytical expression of the uncertainty. The uncertainty adopted by Serpico *et al.* [14] is more empirical: "The overall scale error used in the analysis was chosen to be equal to the lowest experimentally determined ϵ_k for that reaction.… It was added in quadrature to the statistical error in the fits…." Cyburt and Davids [56] used the Markov chain Monte Carlo technique to calculate the uncertainties. Note that in our case, the situation is simpler since we do not fit the shape of the S factor, which comes from theory, but only the normalization factor, and we use the error on the α parameter [Eq. (A6)] provided by MINUIT [102].

3. Our method

From another point of view, the recommended normalization factor can be given by the weighted average of the $\hat{\alpha}_k$ obtained by Eqs. (A2) and (A3) from different experiments (labeled k),

$$\bar{\alpha} = \sum_{k=1}^{N} \frac{\hat{\alpha}_k}{\sigma^2_{\hat{\alpha};k}} \left(\sum_{k=1}^{N} \frac{1}{\sigma^2_{\hat{\alpha};k}} \right)^{-1}. \qquad \text{(A7)}$$

Working out the algebra, starting from Eqs. (A2) and (A3), one finds that this equation is just a rephrasing of Eq. (A4) when no extranormalization error, ϵ_k, has to be introduced. On the contrary, it is easily introduced in Eq. (A7) by the change

$$\sigma^2_{\hat{\alpha};k} \to \sigma^2_{\hat{\alpha};k} + \epsilon^2_k. \qquad \text{(A8)}$$

The error on $\bar{\alpha}$ would normally be given by

$$\sigma^2_{\bar{\alpha}} = \left(\sum\nolimits_k \frac{1}{\sigma^2_{\hat{\alpha};k}} \right)^{-1}. \qquad \text{(A9)}$$

We considered the possibility of applying the rescaling of Cyburt *et al.* [13,99] by $\sqrt{\chi^2}$ to Eq. (A9), together with an extra $N/(N-1)$, in order to obtain a weighted empirical variance

$$\sigma^2_{\bar{\alpha}} = \frac{N}{N-1} \sum_{k=1}^{N} \frac{(\hat{\alpha}_k - \bar{\alpha})^2}{\sigma^2_{\hat{\alpha};k}} \left(\sum_{k=1}^{N} \frac{1}{\sigma^2_{\hat{\alpha};k}} \right)^{-1}. \qquad \text{(A10)}$$

[Apart from the $N/N-1$ factor, this is just Eq. (21) of Cyburt [13].] This has the advantage of converging to the empirical variance $[\sum(X_i - \bar{X})^2/(N-1)]$ when the σ's are all equal or favoring the contributions of the terms with lower σ's if it is not the case. If systematics are negligible, the central values would be the same, but Eq. (A5) would give a larger uncertainty. However, we found that, *after introducing the normalization error with* Eq. (A8), the reduced chi square was always close to unity. Accordingly, we found it unnecessary to inflate the uncertainty by a $\sqrt{\chi^2}$ factor.

APPENDIX B: THE D$(p,\gamma)^3$He DATA

The S factor is related to the total cross section by

$$S(E) = \sigma(E) E \exp\left(\frac{0.810799}{\sqrt{E}} \right) \qquad \text{(B1)}$$

(MeV and barn units). In the following, we detail the experimental data that we considered in this evaluation, in general taken from published tables, but when scanned from a figure, we provide here tables of the extracted numerical values.

The data of Casella *et al.* (LUNA) [22] come from their Table I where "only accidental errors are reported: the systematic uncertainties ranged from 3.6% ($E_{\text{eff}} = 21.23$ keV, highest measured energy) to 5.3% ($E_{\text{eff}} = 2.52$ keV, lowest measured energy) and are negligible in comparison with the accidental errors." We hence adopt $\epsilon = 0.045$ as an average systematic uncertainty.

It was found that NACRE overlooked the overall scaling factor of 1.37 [103] missing in the Schmidt *et al.* [31] data. Here, we follow DAACV and use instead A_0 (multiplied by 4π) from Table II in Schmidt *et al.* [36]. The uncertainties reported in their Table I are statistical only. The systematic error is evaluated in their Sec. II H to be $\epsilon = 0.09$ and is used in their Fig. 13.

The S factor, obtained from Fig. 9 in Ma *et al.* [33], is shown in our Table IV. The systematic uncertainty is estimated to be $\epsilon = 0.09$, but may already be included in the error bars of their Fig. 9.

NACRE used data from Wölfli *et al.* [32] (in German), presumably scanned from their Fig. 6 or from Fig. 1 in Ref. [104], which is a comparison with theory. The lowest energy data point reported by NACRE at E_{CM} is probably an error since the experiment explored the $E_p = 2$–12 MeV range. Only three data points are found below $E_{CM} = 2$ MeV, the limit of the theoretical calculation. In addition, the evaluation of the systematic uncertainty is difficult from the publications.

NACRE [20], NACRE-II [21], and Serpico *et al.* [14] use the data from Geller *et al.* [30]. However, as shown in their Fig. 2 [30] and text, all data are normalized to the Gunn-Irving theoretical cross section [105] at $E_p = 3.07$ MeV. Therefore, we do not use these data for normalization.

NACRE used cross-section data for ^{3}He photodisintegration, scanned from Fig. 2 in Warren *et al.* [26], and

TABLE IV. Data from Ma *et al.* [33].

E_{CM} [MeV]	S [eV b]
0.075	0.685 ± 0.070
0.107	0.708 ± 0.068
0.133	0.956 ± 0.084
0.173	1.26 ± 0.10

TABLE V. Data from Warren *et al.* [26].

E_{CM} [MeV]	σ [μb]	S [eV b]
0.637	3.2 ± 0.3	5.7 ± 0.5
1.465	5.3 ± 0.9	15 ± 2
1.575	5.2 ± 0.6	16 ± 2

TABLE VI. Data from Griffiths *et al.* [24,25].

E_{CM} [MeV]	σ [μb]	S [eV b]
0.015	0.039 ± 0.008	0.43 ± 0.09
0.016	0.044 ± 0.011	0.42 ± 0.10
0.018	0.052 ± 0.009	0.39 ± 0.07
0.020	0.063 ± 0.014	0.38 ± 0.09
0.022	0.077 ± 0.011	0.39 ± 0.06
0.023	0.086 ± 0.011	0.41 ± 0.05
0.024	0.092 ± 0.016	0.41 ± 0.07
0.026	0.12 ± 0.02	0.47 ± 0.07
0.027	0.12 ± 0.02	0.44 ± 0.06
0.028	0.12 ± 0.2	0.44 ± 0.07
0.031	0.15 ± 0.02	0.47 ± 0.06
0.032	0.14 ± 0.02	0.41 ± 0.07
0.183	0.97 ± 0.11	1.18 ± 0.13
0.387	(2.20 ± 0.25)	(3.13 ± 0.36)
0.503	2.71 ± 0.13	4.28 ± 0.21
0.657	3.50 ± 0.38	6.25 ± 0.68
1.167	(4.92 ± 0.50)	(12.16 ± 1.24)

applied a detailed balance theorem to obtain the $d(p,\gamma)^3$He cross section that appears in Table V. There is no information on systematic uncertainty.

NACRE used experimental data from Griffiths *et al.* [24,25], presented here in Table VI. The low energy S factor was obtained by scanning Fig. 6 in Ref. [25] while the high energy cross section is taken from Table I in Ref. [24]. Data between parentheses are relative measurements and are not used in the fits.

DAACV quote the data from Bailey *et al.* [34]. Table VII displays our own scanned data from Fig. 1 of that article by Bailey *et al.* [34]. These data have nothing in common with the presumably erroneous data displayed in Fig. 1(a) of DAACV.

NACRE-II used the data from Table 3 in Bystritsky *et al.* [38]; the systematic uncertainty is less than 8%.

TABLE VII. Data from Bailey *et al.* [34].

E_{CM} [MeV]	σ [μb]	S [eV b]
0.067	0.43 ± 0.06	0.66 ± 0.09
0.092	0.67 ± 0.07	0.88 ± 0.09
0.260	1.55 ± 0.11	1.98 ± 0.14
0.311	1.77 ± 0.12	2.36 ± 0.15
0.342	2.01 ± 0.11	2.75 ± 0.14
0.411	2.26 ± 0.11	3.29 ± 0.16
0.432	2.34 ± 0.08	3.47 ± 0.12
0.462	2.46 ± 0.10	3.75 ± 0.15
0.528	2.69 ± 0.12	4.34 ± 0.19
0.660	3.31 ± 0.19	5.93 ± 0.33
0.727	3.43 ± 0.190	6.45 ± 0.35

Unlike DAACV, we do not use the data of Skopik *et al.* [35] because the energies are well above the limits of our adopted theoretical model.

APPENDIX C: THE D(d,n)^{3}He AND D(d,p)^{3}H DATA

In the range of energy we are interested in, all experiments have measured both of these reaction cross sections. This allows us to perform a test to evaluate the coherence of the data because the ratio of these cross sections is essentially governed by the Coulomb interaction, and as such is weakly dependent of the nuclear model. We take as reference the recent *ab initio* calculation of Arai *et al.* [44]. As mentioned before, the theoretical energy dependence is more accurate than the normalization. Therefore the ratio of both cross sections is expected to be quite reliable and offers a good test of the various experimental data.

The curve in Fig. 15 represents the ratio of theoretical cross sections compared with the data sets to be discussed below. Confidence in this theoretical shape is reinforced by the fact that the most recent directly measured [16] and higher energy [40] experimental data sets follow precisely (except for a few data points) this curve. This can hardly be accidental: even though the model, because of limitations on angular momentum, underestimates the high energy absolute cross sections, the ratio is well reproduced, suggesting that it is indeed independent of the nuclear matrix elements. Obviously, this comparison is of no use to identify systematic errors in normalization that would affect both reactions in the same way. However, deviations from the theoretical ratio may indicate normalization errors in at least one of the reactions.

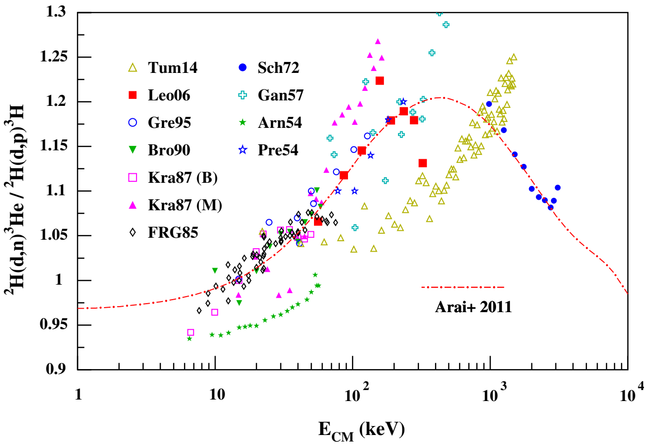

FIG. 15 (color online). Ratios of $d(d,n)^3$He to $d(d,p)^3$H experimental and theoretical S factors from Arai *et al.* [44].

The S factor is related to the total cross section by

$$S(E) = \sigma(E) E \exp\left(\frac{0.992857}{\sqrt{E}}\right). \tag{C1}$$

In the following subsections, we detail the experimental data that we considered in this evaluation.

NACRE and DAACV used the S factor and uncertainties from Schulte *et al.* [40], but the theoretical model does not reach their energy range, and we have to put it aside. This is unfortunate since the ratio of cross sections follow the theoretical ratio (Coulomb only) in Fig. 15, suggesting that the normalizations are correct, or at least differ by the same constant factor.

We considered the Trojan Horse data [17], but the evolution of the ratio of cross sections (Fig. 15) is completely different from the theoretical one. We are not able to tell whether this discrepancy is experimental or is due to the theoretical model used to extract the two-body cross section from the three-body experimental data. However, we note that the discrepancies seen in Fig. 15 and between Figs. 6 and 7 are of the order of 10%. It is not acceptable for the precision required here, but it would be excellent, compared with other indirect methods.

The data from Leonard *et al.* [16] are taken from their Table III, while their Table V provides the error matrix and quote a 2%±1% scale error.

Table 4 in Greife *et al.* [43] provides S factors for the $d(d,p)^3$H reaction below 15 keV; however, their Fig. 1 (a) shows an important screening effect. Consequently, we do not use $E_{CM} \lesssim 15$ keV data for this reaction. We use only the S factor calculated from the cross sections found in their Table 2 [43] whose uncertainties include systematics [solid angles (3%), gas pressure (1%), and calorimetric measurements (1%) (see caption of Table 2)]. Since they dominate over statistical errors, we adopt $\epsilon = 0.033$.

The experiments of Krauss *et al.* [41] took place in Münster ($3 \lesssim E_{CM} \lesssim 50$ keV) and at Bochum ($15 \lesssim E_{CM} \lesssim 163$ keV). We exclude the $E < 15$ keV data because of screening (see above). Table 2 in Krauss *et al.* [41] provides S factors and statistical uncertainties. A normalization error of 6.4% comes from an absolute $d(d,p)^3$H cross section measurement at $E_{CM} = 49.67$ keV, to which a 5% error due to variations in the alignment of beam and jet target profiles has to be added for the Münster data. NACRE added quadratically all these errors. Hence, we use $\epsilon = 0.064$ for the Bochum data and, following the authors, $\epsilon = 0.082$ for the Münster data.

NACRE used the S factor and uncertainties (0.4%–4%) from Table II in Brown and Jarmie [42]. *However, NACRE did not take into account the 1.3% "scale error," dominated by the uncertainty in the* $p + d$ *elastic calibration* leading to $\epsilon = 0.013$.

The article from the "The First Research Group, The First Research Division" [45], written in Chinese, reports on the $d(d,p)^3$H and $d(d,n)^3$He cross-section data, from $E_d = 15$ to 150 keV, which are available in [106] and have been used in Refs. [14,17]. The ratio of cross sections, shown in Fig. 15, follows closely and scatters evenly around the theoretical curve. However, because of our inability to understand the core of the article, and in particular the error budget, we considered these results in our evaluation, but did not use them in our fit.

Preston *et al.* [48] measured the $d(d,p)^3$H and $d(d,n)^3$He cross sections, from $E_d = 156$ to 466 keV. The ratio of the cross section is in good agreement with theory (Fig. 15).

We list here data that may have been used in other evaluations but that we put aside in our evaluation. The results from Bystritsky *et al.* [107] quoted in NACRE-II are not considered as they concern a range of energy where screening is important. The same ($E < 10$ keV) applies to data from Belov *et al.* [108] obtained from [106]. Hofstee *et al.* (a conference proceeding) [109], also quoted in NACRE-II, is not considered either [two data points with large ($\pm 5\% \pm 2\%$) uncertainty]. Davidenko *et al.* [110] quote a 20% uncertainty on $d(d,n)^3$He. Data from Ganeev *et al.* [46] can be obtained from [106]. There is an overlap in energy range for the $d(d,n)^3$He and $d(d,p)^3$H cross-section measurements but the energy steps are different. Hence, we plotted in Fig. 15 the ratio between σ_n *interpolated* experimental values and experimental σ_p values. The resulting values show a large scatter (≈8%) with respect to the theoretical curve. In McNeill and Keyser [111], it is stated (p. 605) that "In addition, errors in calibration and measurement, amounting to a maximum possible value of 20 percent, must be considered," but we do not include these data in our fit. Arnold *et al.* [47] provide $d(d,n)^3$He and $d(d,p)^3$H cross-section data from $E_d = 13$ to 113 keV with a detailed error analysis. Unfortunately, as can be seen in Fig. 15, their σ_n/σ_p ratio is too small by ≈7%. This is apparently due to a systematic error in the $d(d,n)^3$He data (Fig. 4).

APPENDIX D: TABULATED REACTION RATES

See Table VIII.

TABLE VIII. Present recommended D$(p,\gamma)^3$He, D$(d,n)^3$He, and D$(d,p)^3$H rates[a].

	$d(p,\gamma)^3$He	$d(d,n)^3$He	$d(d,p)^3$H			
T [GK]	Recommended rate	$f.u.$	Recommended rate	$f.u.$	Recommended rate	$f.u.$
0.001	4.815×10^{-14}	1.038	1.142×10^{-8}	1.011	1.173×10^{-8}	1.011
0.002	6.409×10^{-9}	1.038	5.470×10^{-5}	1.011	5.609×10^{-5}	1.011
0.003	4.525×10^{-7}	1.038	3.021×10^{-3}	1.011	3.092×10^{-3}	1.011
0.004	4.896×10^{-6}	1.038	3.732×10^{-2}	1.011	3.814×10^{-2}	1.011
0.005	2.444×10^{-5}	1.038	2.212×10^{-1}	1.011	2.257×10^{-1}	1.011
0.006	8.086×10^{-5}	1.038	8.546×10^{-1}	1.011	8.707×10^{-1}	1.011
0.007	2.078×10^{-4}	1.038	2.505×10^{0}	1.011	2.549×10^{0}	1.011
0.008	4.499×10^{-4}	1.038	6.066×10^{0}	1.011	6.164×10^{0}	1.011
0.009	8.619×10^{-4}	1.038	1.278×10^{1}	1.011	1.297×10^{1}	1.011
0.010	1.506×10^{-3}	1.038	2.424×10^{1}	1.011	2.458×10^{1}	1.011
0.011	2.450×10^{-3}	1.038	4.237×10^{1}	1.011	4.290×10^{1}	1.011
0.012	3.767×10^{-3}	1.038	6.936×10^{1}	1.011	7.016×10^{1}	1.011
0.013	5.531×10^{-3}	1.038	1.077×10^{2}	1.011	1.088×10^{2}	1.011
0.014	7.816×10^{-3}	1.038	1.600×10^{2}	1.011	1.615×10^{2}	1.011
0.015	1.070×10^{-2}	1.038	2.291×10^{2}	1.011	2.310×10^{2}	1.011
0.016	1.425×10^{-2}	1.038	3.179×10^{2}	1.011	3.202×10^{2}	1.011
0.018	2.366×10^{-2}	1.038	5.667×10^{2}	1.011	5.698×10^{2}	1.011
0.020	3.659×10^{-2}	1.038	9.310×10^{2}	1.011	9.343×10^{2}	1.011
0.025	8.753×10^{-2}	1.038	2.504×10^{3}	1.011	2.502×10^{3}	1.011
0.030	1.701×10^{-1}	1.038	5.301×10^{3}	1.011	5.276×10^{3}	1.011
0.040	4.476×10^{-1}	1.038	1.568×10^{4}	1.011	1.549×10^{4}	1.011
0.050	8.915×10^{-1}	1.038	3.369×10^{4}	1.011	3.307×10^{4}	1.011
0.060	1.510×10^{0}	1.038	6.013×10^{4}	1.011	5.868×10^{4}	1.011
0.070	2.302×10^{0}	1.038	9.527×10^{4}	1.011	9.246×10^{4}	1.011
0.080	3.265×10^{0}	1.038	1.390×10^{5}	1.011	1.343×10^{5}	1.011
0.090	4.392×10^{0}	1.038	1.912×10^{5}	1.011	1.837×10^{5}	1.011
0.100	5.676×10^{0}	1.038	2.513×10^{5}	1.011	2.404×10^{5}	1.011
0.110	7.109×10^{0}	1.038	3.190×10^{5}	1.011	3.039×10^{5}	1.011
0.120	8.685×10^{0}	1.038	3.938×10^{5}	1.011	3.737×10^{5}	1.011
0.130	1.040×10^{1}	1.038	4.753×10^{5}	1.011	4.493×10^{5}	1.011
0.140	1.224×10^{1}	1.038	5.631×10^{5}	1.011	5.304×10^{5}	1.011
0.150	1.420×10^{1}	1.038	6.568×10^{5}	1.011	6.165×10^{5}	1.011
0.160	1.628×10^{1}	1.038	7.559×10^{5}	1.011	7.072×10^{5}	1.011
0.180	2.076×10^{1}	1.038	9.691×10^{5}	1.011	9.011×10^{5}	1.011
0.200	2.565×10^{1}	1.038	1.200×10^{6}	1.011	1.110×10^{6}	1.011
0.250	3.941×10^{1}	1.038	1.842×10^{6}	1.011	1.682×10^{6}	1.011
0.300	5.505×10^{1}	1.038	2.555×10^{6}	1.011	2.309×10^{6}	1.011
0.350	7.225×10^{1}	1.038	3.318×10^{6}	1.011	2.974×10^{6}	1.011
0.400	9.076×10^{1}	1.038	4.119×10^{6}	1.011	3.663×10^{6}	1.011
0.450	1.104×10^{2}	1.038	4.946×10^{6}	1.011	4.371×10^{6}	1.011
0.500	1.310×10^{2}	1.038	5.792×10^{6}	1.011	5.089×10^{6}	1.011
0.600	1.748×10^{2}	1.038	7.517×10^{6}	1.011	6.543×10^{6}	1.011
0.700	2.212×10^{2}	1.038	9.260×10^{6}	1.011	8.001×10^{6}	1.011
0.800	2.700×10^{2}	1.038	1.100×10^{7}	1.011	9.448×10^{6}	1.011
0.900	3.207×10^{2}	1.038	1.272×10^{7}	1.011	1.087×10^{7}	1.011
1.000	3.729×10^{2}	1.038	1.442×10^{7}	1.011	1.228×10^{7}	1.011
1.250	5.093×10^{2}	1.038	1.850×10^{7}	1.011	1.565×10^{7}	1.011
1.500	6.522×10^{2}	1.038	2.235×10^{7}	1.011	1.882×10^{7}	1.011
1.750	8.000×10^{2}	1.038	2.595×10^{7}	1.012	2.181×10^{7}	1.012
2.000	9.517×10^{2}	1.038	2.932×10^{7}	1.012	2.461×10^{7}	1.012
2.500	1.265×10^{3}	1.038	3.546×10^{7}	1.013	2.976×10^{7}	1.013

(Table continued)

TABLE VIII. (*Continued*)

	$d(p,\gamma)^3$He	$d(d,n)^3$He	$d(d,p)^3$H			
T [GK]	Recommended rate	$f.u.$	Recommended rate	$f.u.$	Recommended rate	$f.u.$
3.000	1.587×10^3	1.038	4.093×10^7	1.014	3.440×10^7	1.014
3.500	1.914×10^3	1.038	4.585×10^7	1.014	3.863×10^7	1.014
4.000	2.244×10^3	1.039	5.031×10^7	1.015	4.251×10^7	1.015
5.000	2.905×10^3	1.040	5.816×10^7	1.016	4.946×10^7	1.016
6.000	3.557×10^3	1.042	6.488×10^7	1.017	5.552×10^7	1.017
7.000	4.194×10^3	1.044	7.072×10^7	1.018	6.077×10^7	1.018
8.000	4.812×10^3	1.046	7.583×10^7	1.018	6.529×10^7	1.018
9.000	5.410×10^3	1.047	8.037×10^7	1.018	6.912×10^7	1.018
10.000	5.988×10^3	1.049	8.437×10^7	1.018	7.228×10^7	1.019

[a] $f.u.$ = uncertainty factor; see Eq. (4.1) and Ref. [49].

[1] G. Hinshaw *et al.*, Astrophys. J. Suppl. Ser. **208**, 19 (2013).

[2] P. A. R. Ade *et al.* (Planck Collaboration XVI), Astron. Astrophys. **571**, A16 (2014).

[3] P. A. R. Ade *et al.* (Planck Collaboration XIII), arXiv:1502.01589.

[4] E. Aver, K. A. Olive, and E. D. Skillman, J. Cosmol. Astropart. Phys. 07 (2015) 011.

[5] A. Coc, J.-P. Uzan, and E. Vangioni, J. Cosmol. Astropart. Phys. 10 (2014) 050.

[6] R. H. Cyburt, B. D. Fields, and K. A. Olive, J. Cosmol. Astropart. Phys. 11 (2008) 012.

[7] A. Coc and E. Vangioni, J. Phys. Conf. Ser. **202**, 012001 (2010).

[8] R. H. Cyburt, B. D. Fields, K. A. Olive, and T.-H. Yeh, arXiv:1505.01076.

[9] B. D. Fields, Annu. Rev. Nucl. Part. Sci. **61**, 47 (2011).

[10] A. Coc, M. Pospelov, J.-P. Uzan, and E. Vangioni, Phys. Rev. D **90**, 085018 (2014).

[11] X. Fu, A. Bressan, P. Molaro, and P. Marigo, Mon. Not. R. Astron. Soc. **452**, 3256 (2015).

[12] F. Hammache *et al.*, Phys. Rev. C **88**, 062802(R) (2013).

[13] R. H. Cyburt, Phys. Rev. D **70**, 023505 (2004).

[14] P. D. Serpico, S. Esposito, F. Iocco, G. Mangano, G. Miele, and O. Pisanti, J. Cosmol. Astropart. Phys. 12 (2004) 010.

[15] P. Descouvemont, A. Adahchour, C. Angulo, A. Coc, and E. Vangioni-Flam, At. Data Nucl. Data Tables **88**, 203 (2004); http://pntpm.ulb.ac.be/bigbang/.

[16] D. S. Leonard, H. J. Karwowski, C. R. Brune, B. M. Fisher, and E. J. Ludwig, Phys. Rev. C **73**, 045801 (2006).

[17] A. Tumino, R. Sparta, C. Spitaleri, A. M. Mukhamedzhanov, and S. Typel, Astrophys. J. **785**, 96 (2014).

[18] E. G. Adelberger *et al.*, Rev. Mod. Phys. **83**, 195 (2011).

[19] E. Di Valentino, C. Gustavino, J. Lesgourgues, G. Mangano, A. Melchiorri, G. Miele, and O. Pisanti, Phys. Rev. D **90**, 023543 (2014).

[20] C. Angulo *et al.*, Nucl. Phys. **A656**, 3 (1999); http://pntpm.ulb.ac.be/Nacre/nacre.htm.

[21] Y. Xu, K. Takahashi, S. Goriely, M. Arnould, M. Ohta, and H. Utsunomiya, Nucl. Phys. **A918**, 61 (2013).

[22] C. Casella *et al.*, Nucl. Phys. **A706**, 203 (2002).

[23] K. M. Nollett and S. Burles, Phys. Rev. D **61**, 123505 (2000).

[24] G. M. Griffiths, E. A. Larson, and L. P. Robertson, Can. J. Phys. **40**, 402 (1962).

[25] G. M. Griffiths, M. Lal, and C. D. Scarfe, Can. J. Phys. **41**, 724 (1963).

[26] J. B. Warren, K. L. Erdman, L. P. Robertson, D. A. Axen, and J. R. Macdonald, Phys. Rev. **132**, 1691 (1963).

[27] B. L. Berman, L. J. Koester, Jr., and J. H. Smith, Phys. Rev. **133**, B117 (1964).

[28] V. N. Fetisov, A. N. Gorbunov, and A. T. Varflomeev, Nucl. Phys. **71**, 305 (1965).

[29] J. R. Stewart, R. C. Morrison, and J. S. O'Connell, Phys. Rev. **138**, B372 (1965).

[30] K. N. Geller, E. G. Muirhead, and L. D. Cohen, Nucl. Phys. **A96**, 397 (1967).

[31] G. J. Schmid, R. M. Chastler, C. M. Laymon, and H. R. Weller, Phys. Rev. C **52**, R1732 (1995).

[32] W. Wölfli, R. Bösch, J. Lang, R. Müller, and P. Marmier, Helv. Phys. Acta **40**, 946 (1967).

[33] L. Ma, H. J. Karwowski, C. R. Brune, Z. Ayer, T. C. Black, J. C. Blackmon, E. J. Ludwig, M. Viviani, A. Kievsky, and R. Schiavilla, Phys. Rev. C **55**, 588 (1997).

[34] G. M. Bailey, G. M. Griffiths, M. A. Olivio, and R. L. Helmer, Can. J. Phys. **48**, 3059 (1970).

[35] D. M. Skopik, H. R. Weller, N. R. Roberson, and S. A. Wender, Phys. Rev. C **19**, 601 (1979).

[36] G. J. Schmid, B. J. Rice, R. M. Chasteler, M. A. Godwin, G. C. Kiang, L. L. Kiang, C. M. Laymo, R. M. Prior, D. R. Tilley, and H. R. Weller, Phys. Rev. C **56**, 2565 (1997).

[37] M. Viviani, A. Kievsky, L. E. Marcucci, S. Rosati, and R. Schiavilla, Phys. Rev. C **61**, 064001 (2000); L. E. Marcucci, M. Viviani, R. Schiavilla, A. Kievsky, and S. Rosati, Phys. Rev. C **72**, 014001 (2005); L. E. Marcucci (private communication).

[38] V. M. Bystritsky *et al.*, Nucl. Instrum. Methods Phys. Res., Sect. A **595**, 543 (2008).

[39] R. Cooke, M. Pettini, R. A. Jorgenson, M. T. Murphy, and C. C. Steidel, Astrophys. J. **781**, 31 (2014).

[40] R. L. Schulte, M. Cosack, A. W. Obst, and J. L. Weil, Nucl. Phys. **A192**, 609 (1972).

[41] A. Krauss, H. W. Becker, H. P. Trautvetter, C. Rolfs, and K. Brand, Nucl. Phys. **A465**, 150 (1987).

[42] R. E. Brown and N. Jarmie, Phys. Rev. C **41**, 1391 (1990).

[43] U. Greife, F. Gorris, M. Junker, C. Rolfs, and D. Zahnow, Z. Phys. A **351**, 107 (1995).

[44] K. Arai, S. Aoyama, Y. Suzuki, P. Descouvemont, and D. Baye, Phys. Rev. Lett. **107**, 132502 (2011).

[45] First Research Group, Chin. J. Nucl. Phys. **9**, 723 (1985).

[46] A. S. Ganeev, A. M. Govorov, G. M. Osetinskij, A. N. Rakivnenko, I. V. Sizov, and V. S. Siksin, Sov. At. En., Suppl. **1957**, 21 (1957).

[47] W. R. Arnold, J. A. Phillips, G. A. Sawyer, E. J. Stovall, Jr., and J. L. Tuck, Phys. Rev. **93**, 483 (1954).

[48] G. R. Preston, P. F. D. Shaw, and S. A. Young, Proc. R. Soc. A **226**, 206 (1954).

[49] R. Longland, C. Iliadis, A. E. Champagne, J. R. Newton, C. Ugalde, A. Coc, and R. Fitzgerald, Nucl. Phys. **A841**, 1 (2010).

[50] C. Iliadis, R. Longland, A. Coc, F. X. Timmes, and A. E. Champagne, J. Phys. G **42**, 034007 (2015).

[51] D. J. Fixsen, Astrophys. J. **707**, 916 (2009).

[52] G. Mangano, G. Miele, S. Pastor, T. Pinto, O. Pisanti, and P. D. Serpico, Nucl. Phys. **B729**, 221 (2005).

[53] O. Pisanti, A. Cirillo, S. Esposito, F. Iocco, G. Mangano, G. Miele, and P. D. Serpico, Comput. Phys. Commun. **178**, 956 (2008).

[54] T. Bania, R. Rood, and D. Balser, Nature (London) **415**, 54 (2002).

[55] L. Sbordone *et al.*, Astron. Astrophys. **522**, A26 (2010).

[56] R. H. Cyburt and B. Davids, Phys. Rev. C **78**, 064614 (2008).

[57] R. J. deBoer, J. Görres, K. Smith, E. Uberseder, M. Wiescher, A. Kontos, G. Imbriani, A. Di Leva, and F. Strieder, Phys. Rev. C **90**, 035804 (2014).

[58] R. V. Wagoner, Astrophys. J. Suppl. Ser. **18**, 247 (1969).

[59] S. Q. Hou, J. J. He, S. Kubono, and Y. S. Chen, Phys. Rev. C **91**, 055802 (2015).

[60] K. A. Olive *et al.* (Particle Data Group), Chin. Phys. C **38**, 090001 (2014); http://pdg.lbl.gov.

[61] M. Pettini and M. Cooke, Mon. Not. R. Astron. Soc. **425**, 2477 (2012).

[62] S. Riemer-Sørensen, J. K. Webb, N. Crighton, V. Dumont, K. Ali, S. Kotuš, M. Bainbridge, M. T. Murphy, and R. Carswell, Mon. Not. R. Astron. Soc. **447**, 2925 (2015).

[63] P. Noterdaeme, S. López, V. Dumont, C. Ledoux, P. Molaro, and P. Petitjean, Astron. Astrophys. **542**, L33 (2012).

[64] J. Tumlinson, A. L. Malec, R. F. Carswell, M. T. Murphy, R. Buning, N. Milutinovic, S. L. Ellison, J. X. Prochaska, R. A. Jorgenson, W. Ubachs, and A. M. Wolfe, Astrophys. J. Lett. **718**, L156 (2010).

[65] R. Srianand, N. Gupta, P. Petitjean, P. Noterdaeme, and C. Ledoux, Mon. Not. R. Astron. Soc. **405**, 1888 (2010).

[66] A. V. Ivanchik, P. Petitjean, S. A. Balashev, R. Srianand, D. A. Varshalovich, C. Ledoux, and P. Noterdaeme, Mon. Not. R. Astron. Soc. **404**, 1583 (2010).

[67] S. A. Balashev, A. V. Ivanchik, and D. A. Varshalovich, Astron. Lett. **36**, 761 (2010).

[68] F. Le Petit, B. Barzel, O. Biham, E. Roueff, and J. Le Bourlot, Astron. Astrophys. **505**, 1153 (2009).

[69] T. Prodanović, G. Steigman, and B. D. Fields, Mon. Not. R. Astron. Soc. **406**, 1108 (2010).

[70] J. L. Linsky *et al.*, Astrophys. J. **647**, 1106 (2006).

[71] B. D. Savage, N. Lehner, A. Fox, B. Wakker, and K. Sembach, Astrophys. J. **659**, 1222 (2007).

[72] F. Daigne, K. A. Olive, J. Silk, F. Stoehr, and E. Vangioni, Astrophys. J. **647**, 773 (2006).

[73] E. Rollinde, E. Vangioni, D. Maurin, K. A. Olive, F. Daigne, J. Silk, and F. H. Vincent, Mon. Not. R. Astron. Soc. **398**, 1782 (2009).

[74] E. Vangioni, K. A. Olive, T. Prestegard, J. Silk, P. Petitjean, and V. Mandic, Mon. Not. R. Astron. Soc. **447**, 2575 (2015).

[75] W. H. Press and P. Schechter, Astrophys. J. **187**, 425 (1974).

[76] J. S. B. Wyithe and A. Loeb, Astrophys. J. Lett. **588**, L69 (2003).

[77] P. A. Oesch *et al.*, Astrophys. J. **786**, 108 (2014).

[78] R. J. Bouwens *et al.*, Astrophys. J. **795**, 126 (2014).

[79] M. Trenti, R. Perna, and S. Tacchella, Astrophys. J. Lett. **773**, L22 (2013).

[80] P. S. Behroozi and J. Silk, Astrophys. J. **799**, 32 (2015).

[81] P. S. Behroozi, R. H. Wechsler, and C. Conroy, Astrophys. J. **770**, 57 (2013).

[82] M. D. Kistler, H. Yuksel, and A. M. Hopkins, arXiv:1305.1630.

[83] E. E. Salpeter, Astrophys. J. **121**, 161 (1955).

[84] G. Chabrier, P. Hennebelle, and S. Charlot, Astrophys. J. **796**, 75 (2014).

[85] T. Prodanović, G. Steigman, and B. Fields, *Proc. Sci.* (NIC XI) 105.

[86] C. Chiappini, A. Renda, and F. Matteucci, Astron. Astrophys. **395**, 789 (2002).

[87] E. Vangioni-Flam, K. A. Olive, B. D. Fields, and M. Cassé, Astrophys. J. **585**, 611 (2003).

[88] K. A. Olive, P. Petitjean, E. Vangioni, and J. Silk, Mon. Not. R. Astron. Soc. **426**, 1427 (2012).

[89] M. Kusakabe, M.-K. Cheoun, and K. S. Kim, Phys. Rev. D **90**, 045009 (2014).

[90] M. H. Reno and D. Seckel, Phys. Rev. D **37**, 3441 (1988).

[91] K. Jedamzik, Phys. Rev. D **70**, 063524 (2004).

[92] D. Albornoz Vásquez, A. Belikov, A. Coc, J. Silk, and E. Vangioni, Phys. Rev. D **86**, 063501 (2012).

[93] R. H. Cyburt, J. Ellis, B. D. Fields, F. Luo, K. A. Olive, and V. C. Spanos, J. Cosmol. Astropart. Phys. 05 (2013) 014.

[94] N. Chakraborty, B. D. Fields, and K. A. Olive, Phys. Rev. D **83**, 063006 (2011).

[95] A. Coc, S. Goriely, Y. Xu, M. Saimpert, and E. Vangioni, Astrophys. J. **744**, 158 (2012).

[96] O. S. Kirsebom and B. Davids, Phys. Rev. C **84**, 058801 (2011).

[97] A. Coc, P. Descouvemont, K. Olive, J.-P. Uzan, and E. Vangioni, Phys. Rev. D **86**, 043529 (2012).

[98] L. E. Marcucci, G. Mangano, A. Kievsky, and M. Viviani, arXiv:1510.07877.

[99] R. H. Cyburt, B. Fields, and K. A. Olive, New Astron. **6**, 215 (2001).

[100] G. D'Agostini, Nucl. Instrum. Methods Phys. Res., Sect. A **346**, 306 (1994).

[101] D. Schürmann, L. Gialanella, R. Kunz, and F. Strieder, Phys. Lett. B **711**, 35 (2012).

[102] F. James, CERN Report No. CERN-D-506, 1994, available at https://inspirehep.net/record/1258343/files/minuit.pdf.

[103] G. J. Schmid *et al.*, Phys. Rev. Lett. **76**, 3088 (1996).

[104] W. Wölfli, R. Bösch, J. Lang, R. Müller, and P. Marmier, Phys. Lett. **22**, 75 (1966).

[105] J. C. Gunn and J. Irving, Philos. Mag. **42**, 1353 (1951).

[106] http://www.nndc.bnl.gov/exfor/exfor.htm.

[107] V. M. Bystritsky *et al.*, Eur. Phys. J. A **36**, 151 (2008); Nucl. Phys. **A889**, 93 (2012).

[108] A. S. Belov, V. E. Kusik, and Yu. V. Ryabov, Nuovo Cimento Soc. Ital. Fis. **103A**, 1647 (1990).

[109] M. A. Hofstee, A. K. Pallone, F. E. Cecil, J. A. McNeil, and C. S. Galovich, Nucl. Phys. **A688**, 527 (2001).

[110] V. A. Davidenko, A. M. Kucher, I. S. Pogrebov, and Ju. F. Tuturov, Sov. At. En., Suppl. **1957**, 7 (1957).

[111] K. G. McNeill and G. M. Keyser, Phys. Rev. **81**, 602 (1951).